Modelings, Simulations, Measurements and Comparisons of Monopole-Type Blade Antennas

by

Kaiyue Zhang

A Thesis Presented in Partial Fulfillment
of the Requirement for the Degree
Master of Science

Approved May 2014 by the
Graduate Supervisory Committee:

Constantine A. Balanis, Chair
George Pan
James T. Aberle

ARIZONA STATE UNIVERSITY

August 2014

ABSTRACT

Two commercial blade antennas for aircraft applications are investigated. The computed results are compared with measurements performed in the ASU Electro-Magnetic Anechoic Chamber (EMAC). The antennas are modeled as mounted on a 13-inch diameter circular ground plane, which corresponds to that of the measurements.

Two electromagnetic modeling codes are used in this project to model the antennas and predict their radiation and impedance characteristics: FEKO and WIPL-D Pro. A useful tool of WIPL-D Pro, referred to as WIPL-D Pro CAD, has proven to be convenient for modeling complex geometries. The classical wire monopole was also modeled using high-frequency methods, GO and GTD/UTD, mounted on both a rectangular and a circular ground plane. A good agreement between the patterns of this model and FEKO has been obtained.

The final versions of the solvers used in this work are FEKO (Suit 6.2), WIPL-D Pro v11 and WIPL-D Pro CAD 2013. Features of the simulation solvers are presented and compared.

Simulation results of FEKO and WIPL-D Pro have good agreements with the measurements for radiation and impedance characteristics. WIPL-D Pro has a much higher computational efficiency than FEKO.

TABLE OF CONTENTS

Page

LIST OF FIGURES

Figure Page

Figure Page

Figure Page

Chapter 1

INTRODUCTION

A monopole antenna generally is a class of RF antenna consisting of a straight vertical conductor, fed by a transmission line between the lower end of the monopole and a conductive surface (ground plane) [9]. A blade antenna often is a monopole type of an antenna covered with a trapezoidal radome. The word "radome" is an acronym coined from radar dome. Most of the radomes are utilized and designed for aerodynamic purposes. Therefore, a blade antenna is a good candidate for communication systems on aircrafts [8].

Two different commercial blade antennas designed for aircraft applications were purchased for this thesis project. One operates at C band (5.4 - 5.9 GHz), the other operates at S band (2.35 - 2.45 GHz).

The radiation patterns and impedance characteristics of the two blade antennas were measured in the ASU ElectroMagnetic Anechoic Chamber (EMAC) facility. The antennas were modeled by two different simulation codes, their electromagnetic characteristics were computed, and the predicted characteristics were compared with the measurements.

The research aims of this project can be described as follows:

- Learn to use WIPL-D and FEKO simulation codes.
- Use WIPL-D and FEKO to model two commercial blade antennas, including their radomes.
- Verify radiation patterns and impedance characteristics of commercial blade antennas with measurements.

- Simplify the CAD models for future applications.

1.1 Aircraft Principal Planes

Before introducing the blade antennas, several basic concepts of principal axes and principal planes need to be addressed.

A three-dimensional coordinate system of an aircraft is defined through its center of gravity, a point which is the average location of its mass. Yaw axis, roll axis and pitch axis are defined to be the three principal axes of this coordinate system. Each one of the three axes is perpendicular to the other two (mutually orthogonal). The orientation of the aircraft is defined by the amount of rotation of its parts along these principal axes [1].

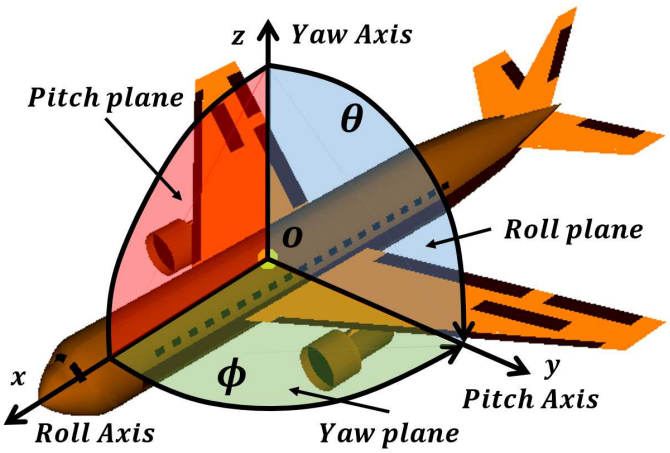

Figure 1.1: Aircraft principal axes and planes.

The three principal axes are illustrated in Figure 1.1. The yaw axis is defined to be perpendicular to the plane of the fuselage, starting from the center of gravity towards the top of the aircraft. A yaw motion is a swing movement of the aircraft's nose from side to side. The roll axis is defined to be perpendicular to the yaw axis and wings, which starts from the center of the gravity towards the nose of the aircraft. A

rolling motion is a rotary movement around the roll axis. A pitch axis is defined to be perpendicular to the other two axes, starting from the center of gravity towards the wing tip.

The principal planes are defined to be perpendicular to their corresponding axes. The yaw plane, also referred to as the azimuth plane, is perpendicular to the yaw axis. The yaw plane splits the aircraft into top half and bottom half. The pitch plane, also referred to as the $\phi = 0^\circ$ elevation plane, is perpendicular to the pitch axis and yaw plane. The pitch plane divides the aircraft into left half and right half. The roll plane, also referred to as the $\phi = 90^\circ$ elevation plane, is perpendicular to other two principal planes. The roll plane cut the aircraft into front half and rear half.

In most cases, the comparisons of radiation patterns between simulation results and measurements in these three principal planes are sufficient. If the simulation results and measurements have a good agreement in the principal planes, we can presume that the simulation results and measurements have good agreements in all directions.

1.2 Quarter-Wavelength Monopole Antenna

Before introducing the commercial blade antennas, basic concepts of quarter-wavelength monopole ($l = \lambda/4$) antennas need to be addressed. Simulation results of a monopole mounted on a perfect electric conductor (PEC) plane, using diffraction theory, are indicated in this section.

A quarter-wavelength monopole mounted on a ground plane (Figure 1.2), and fed by a coaxial cable is widely used in practice [5]. When the dimension of the ground plane is finite, diffraction from the edges need to be considered. The method of two-point diffraction will be investigated in the later portion of this section.

When the ground plane is an infinite PEC plane, image theory can be used for

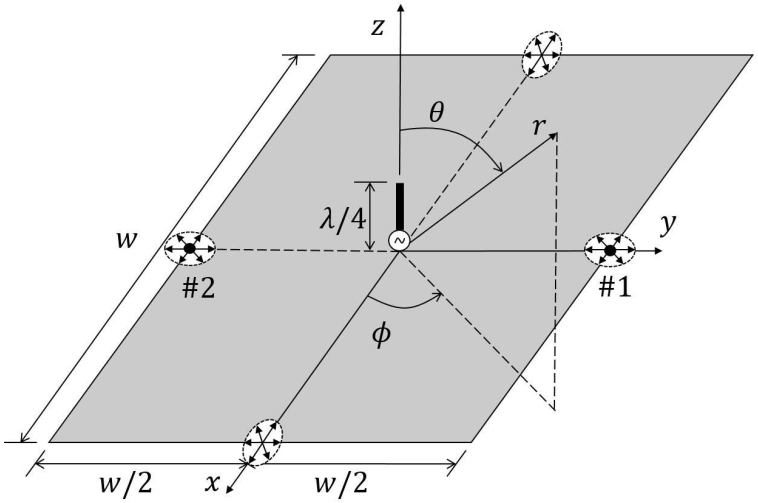

(a)

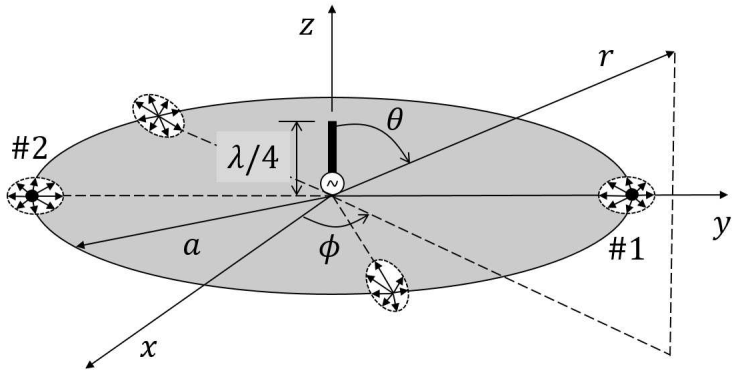

(b)

Figure 1.2: A Quarter-wavelength vertical monopole antenna mounted on PEC ground plane. (a) Square (b) Circular.

the radiation pattern analysis. It introduces a $\lambda/4$ image and forms an ideal half-wavelength ($l = \lambda/2$) dipole in free space, which is fed in the center. To be emphasized, the equivalent $\lambda/2$ dipole provides correct field values only above the ground plane ($z \geq 0, 0 \leq \theta \leq \pi/2$) (Figure 1.2). The far-zone electric and magnetic fields for a quarter-length monopole antenna mounted on a infinite PEC ground plane are represented by [5]

$$E_\theta \backsimeq j\eta \frac{I_0 e^{-jkr}}{2\pi r} \frac{\cos\left(\frac{\pi}{2}\cos\theta\right)}{\sin\theta} \tag{1.1}$$

$$H_\phi \backsimeq j \frac{I_0 e^{-jkr}}{2\pi r} \frac{\cos\left(\frac{\pi}{2}\cos\theta\right)}{\sin\theta} \tag{1.2}$$

The input impedance of a $\lambda/4$ monopole antenna above a ground plane is equal to half of the impedance of an isolated $\lambda/2$ dipole in free space. There is no significant difference between the impedance values of a monopole mounted on a metallic ground plane and an ideal PEC plane [5].

$$\begin{aligned} Z_{im}\,(monopole) &= \frac{1}{2} Z_{im}\,(dipole) \\ &= \frac{1}{2}\,[73 + j42.5] \\ &= 36.5 + j21.25 \end{aligned} \tag{1.3}$$

The amplitude radiation properties of a $\lambda/4$ monopole antenna mounted on an infinite ground plane differ from the monopole above a finite ground plane. There are several techniques of predicting these properties [6]. The physical optics (PO) method provides an approximate current density induced on the surface of an object with finite dimensions. The integral equations (IE) with use of method of moments (MoM) solves the induced current density in the form of an integral equation [6]. Once the current density is obtained, the field scattered by the object can be calculated by radiation integrals. The MoM is a universal technique in FEKO [2] and WIPL-D [3].

Geometrical Optics (GO) is an approximate method developed to analyze the propagation of sufficiently high-frequency light where the the wave nature of light is

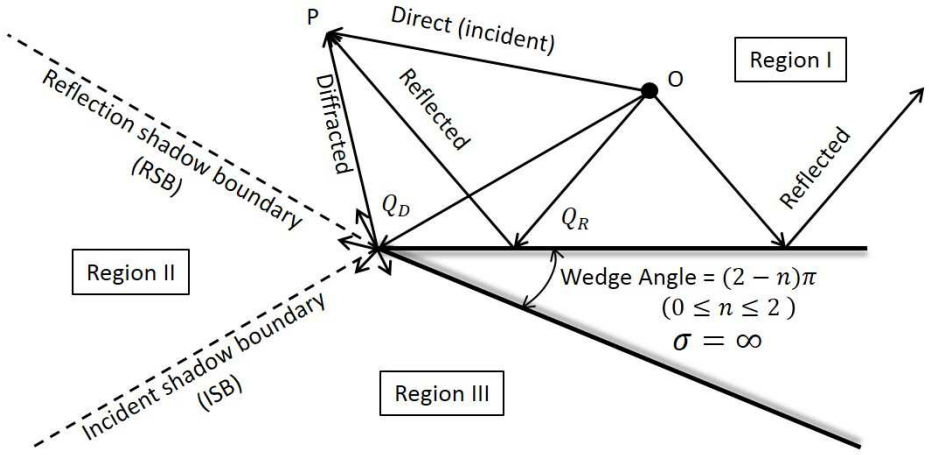

Figure 1.3: Region separation of a line source near a two-dimensional conducting wedge.

not necessarily considered [6]. Incident, reflected and refracted fields are propagating along rays. For reflection problems, like this project, GO approximates the reflected fields based on Snell's law of reflection. When GO rays, incident and reflected, impinge on a finite size structure shadow boundaries are formed and divide the space into illuminated and shadow regions. Figure 1.3 illustrates a reflection problem; that an infinite line source (either electric or magnetic) near a two-dimensional PEC wedge. GO accounts only for incident and reflected rays. Therefore, the space is divided into three regions separated by two shadow boundaries, incident and reflected, and the wedge. The incident field exists in both regions, I and II. The reflected field exists only in region I. No rays are present in region III. This phenomenon introduces discontinuities in the electromagnetic field; however, the actual fields must always be continuous.

The geometrical theory of diffraction (GTD) is an extension of geometrical optics (GO) which accounts for diffraction from the edges of a structure [7], as shown in

Figure 1.3. Like the traditional GO method, GTD assumes that light travels along rays. In addition to the usual GO rays, GTD introduces diffracted rays. By adding diffracted fields, shadow boundaries (discontinuities) are removed and the radiation patterns are improved over the entire space [6]. The total field is then computed as [6]

$$\mathbf{E}^{total} = \mathbf{E}^{GO} + \mathbf{E}^{d} \tag{1.4a}$$

$$\mathbf{E}^{d}(s) = \mathbf{E}^{i}(Q_D) \cdot \bar{\mathbf{D}} A(s', s)\, e^{-j\beta s} \tag{1.4b}$$

where $\mathbf{E}^d$ is the diffracted field, s' and s are the distance along the ray pathes, $\bar{\mathbf{D}}$ is the dyadic diffraction coefficient, A is the spatial attenuation (spreading, divergence) factor and $e^{-j\beta s}$ is the phase factor.

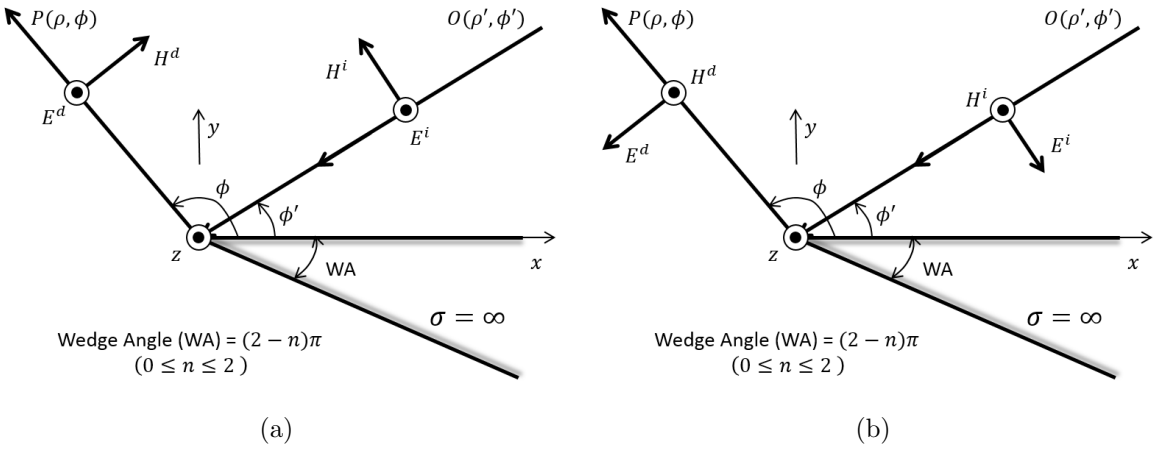

Figure 1.4: Polarization of incident and diffracted fields. (a) Soft (TM) polarization (b) Hard (TE) polarization.

A compact dyadic diffraction coefficient for obliquely incident electromagnetic waves on a perfectly conducting edge is obtained by the uniform geometrical theory of diffraction [6], (UTD) [10]. The superscripts in the equations, s and h, represent

the soft and hard polarizations (Figure 1.4).

$$D_{s,h}(\rho,\phi,\phi',n) = D^i(\rho,\phi-\phi',n) \mp D^r(\rho,\phi+\phi',n) = -\frac{e^{-j\pi/4}}{2n\sqrt{2\pi\beta}}$$
$$\times \left(\{\cot\left[\frac{\pi+(\phi-\phi')}{2n}\right] F[\beta\rho g^+(\phi-\phi')] + \cot\left[\frac{\pi-(\phi-\phi')}{2n}\right] F[\beta\rho g^-(\phi-\phi')]\}\right.$$
$$\left. \mp \{\cot\left[\frac{\pi+(\phi+\phi')}{2n}\right] F[\beta\rho g^+(\phi+\phi')] + \cot\left[\frac{\pi-(\phi+\phi')}{2n}\right] F[\beta\rho g^-(\phi+\phi')]\}\right) \tag{1.5a}$$

$$F[\beta\rho g^+(\phi-\phi')] = 2j\sqrt{\beta\rho g^+(\phi-\phi')}e^{+j\beta\rho g^+(\phi-\phi')}\int_{\sqrt{\beta\rho g^+(\phi-\phi')}}^{\infty} e^{-j\tau^2}\,d\tau \tag{1.5b}$$

$$F[\beta\rho g^-(\phi-\phi')] = 2j\sqrt{\beta\rho g^-(\phi-\phi')}e^{+j\beta\rho g^-(\phi-\phi')}\int_{\sqrt{\beta\rho g^-(\phi-\phi')}}^{\infty} e^{-j\tau^2}\,d\tau \tag{1.5c}$$

$$F[\beta\rho g^+(\phi+\phi')] = 2j\sqrt{\beta\rho g^+(\phi+\phi')}e^{+j\beta\rho g^+(\phi+\phi')}\int_{\sqrt{\beta\rho g^+(\phi+\phi')}}^{\infty} e^{-j\tau^2}\,d\tau \tag{1.5d}$$

$$F[\beta\rho g^-(\phi+\phi')] = 2j\sqrt{\beta\rho g^-(\phi+\phi')}e^{+j\beta\rho g^-(\phi+\phi')}\int_{\sqrt{\beta\rho g^-(\phi+\phi')}}^{\infty} e^{-j\tau^2}\,d\tau \tag{1.5e}$$

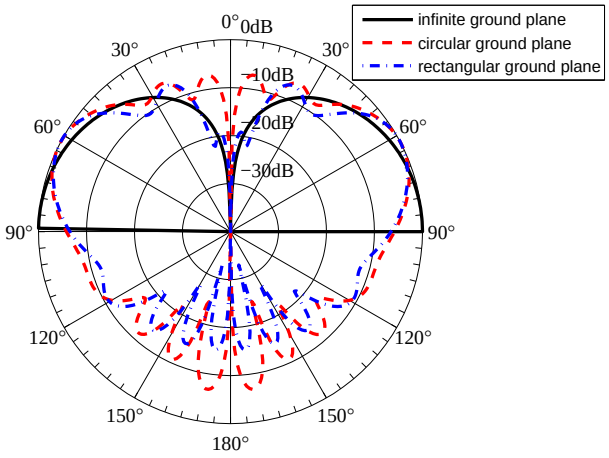

Figure 1.5: Normalized radiation patterns of a $\lambda/4$ monopole mounted on ground planes.

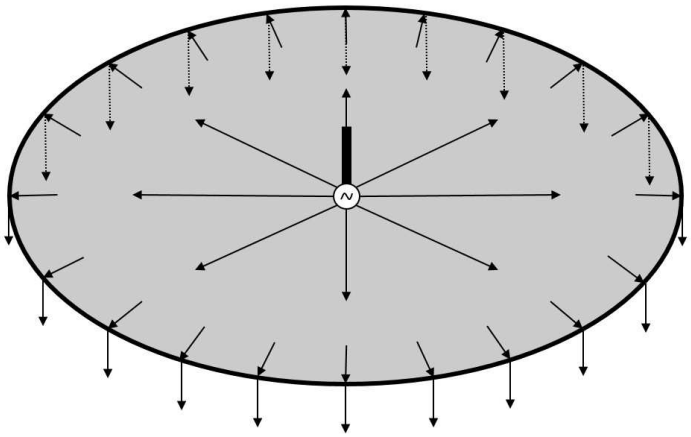

Figure 1.6: The rim of the circular ground plane acting as a ring radiator.

Figure 1.5 is the comparison of radiation patterns of $\lambda/4$ monopoles mounted on different ground planes, as predicted using the Integral Equation (IE) along with the Method of Moments (MoM) option of FEKO [2]. The black solid line represents of the patterns above an infinite ground plane. No field exists below the plane. For the finite ground plane cases, the red dashed and the blue dotted dashed lines, radiation exists in all directions because of the contributions due to diffraction for the edges. The width of the square plate is as long as the circular plate's diameter (Figure 1.2). Due to the rim of the ground plane acting as a ring radiator (Figure 1.6), the circular ground plane case has stronger radiation (around 10 dB), compared to that of the square ground plane, near the symmetry axis ($\theta = 0^\circ$ and 180°).

For the monopole mounted on a square ground plane, illustrated in Figure 1.2 (a), the total field can be approximated by the summation of GO fields (incident and reflected) and diffractions from two edges (#1 and #2) [6]. The GO field is represented by

$$E_{\theta G}(r,\theta) = E_0 \left[\frac{\cos\left(\frac{\pi}{2}\cos\theta\right)}{\sin\theta} \right] \qquad 0 \le \theta \le \pi/2 \tag{1.6}$$

while the diffracted field from edge #1 can be represented by

$$E^d_{\theta 1} = +E^i(Q_1) D_h \left(L, \xi_1^{\pm}, \beta_0' = \frac{\pi}{2}, n = 2\right) A_1(\mathrm{w}, r_1) e^{-j\beta r_1} \tag{1.7}$$

where $\xi_1^{\pm} = \psi_1 \pm \psi_0$ and β_0' is the incident angle on the edge of the ground plane ($\beta_0' = \pi/2$ for normal incidence two-point diffraction). The total field can be assumed to radiate from the base of the monopole. Based on this approximation, the incident field at the points of diffraction can be represented by

$$E^i(Q_1) = \frac{1}{2} E_{\theta G}\left(r = \frac{\mathrm{w}}{2}, \theta = \frac{\pi}{2}\right) = \frac{E_0}{2} \frac{e^{-j\beta \mathrm{w}/2}}{\mathrm{w}/2} \tag{1.8a}$$

while the diffracted coefficient can be expressed as

$$D_h \left(L, \xi_1^{\pm}, \beta_0' = \frac{\pi}{2}, n = 2\right) = D^i \left(L, \xi_1^{-}, n = 2\right) + D^r \left(L, \xi_1^{+}, n = 2\right) \tag{1.8b}$$

Since the observations are made in the far field and the incident angle ψ_0 is zero degrees when the ray is radiating from the source towards edge #1, then according to the geometry of Figure 1.7

$$L = s' \sin^2 \beta_0' = \tfrac{\mathrm{w}}{2} \tag{1.9}$$

$$A_1(\mathrm{w}, r_1) = \tfrac{\sqrt{s'}}{s} = \sqrt{\tfrac{\mathrm{w}/2}{r_1}} \tag{1.10}$$

$$\xi_1^{\pm} = \psi_1 \pm \psi_0 = \theta + \tfrac{\pi}{2} = \xi_1 \tag{1.11}$$

Therefore

$$\begin{aligned} D_h \left(L, \xi_1^{\pm}, \beta_0' = \frac{\pi}{2}, n = 2\right) &= 2D^i \left(L, \xi_1^{-}, n = 2\right) \\ &= 2D^r \left(L, \xi_1^{+}, n = 2\right) \end{aligned} \tag{1.12}$$

Substituting all these parts in (1.7), the total diffracted field from edge #1 can be written as [6]

$$\begin{aligned} E^d_{\theta 1}(\theta) &= +\frac{E_0}{2} \frac{e^{-j\beta \mathrm{w}/2}}{\mathrm{w}/2} 2D^{i,r}\left(\frac{\mathrm{w}}{2}, \theta + \frac{\pi}{2}, n = 2\right) \frac{\sqrt{\mathrm{w}/2}}{r_1} e^{-j\beta r_1} \\ &= +E_0 \left[\frac{e^{-j\beta \mathrm{w}/2}}{\sqrt{\mathrm{w}/2}} D^{i,r}\left(\frac{\mathrm{w}}{2}, \theta + \frac{\pi}{2}, n = 2\right)\right] \frac{e^{-j\beta r_1}}{r_1} \end{aligned} \tag{1.13a}$$

$$E_{\theta 1}^{d}(\theta) = +E_0 V_B^{i,r}\left(\frac{\mathrm{w}}{2}, \theta + \frac{\pi}{2}, n = 2\right)\frac{e^{-j\beta r_1}}{r_1} \tag{1.13b}$$

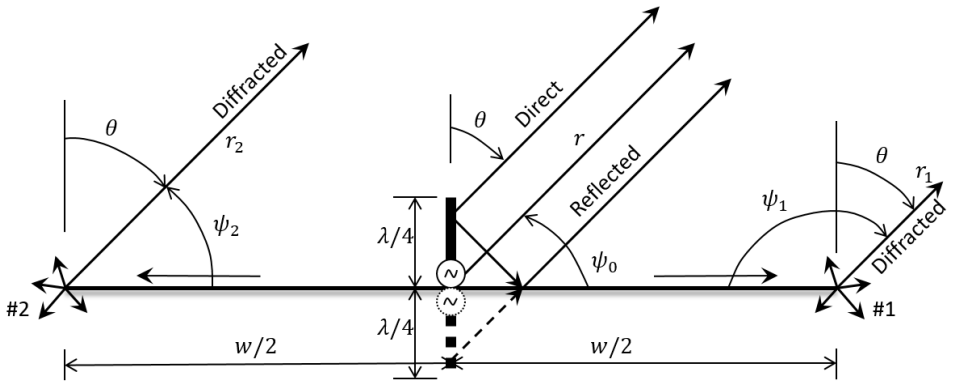

Figure 1.7: Reflection and diffraction mechanisms of a vertical monopole mounted on a PEC square ground plane.

Similarly, the diffracted field from edge #2 according to the geometry of Figure 1.7 can be written as [6]

$$E_{\theta 2}^{d}(\theta) = -E_0\left[\frac{e^{-j\beta \mathrm{w}/2}}{\sqrt{\mathrm{w}/2}} D^{i,r}\left(\frac{\mathrm{w}}{2}, \xi_2, n = 2\right)\right]\frac{e^{-j\beta r_2}}{r_2} \tag{1.14a}$$

$$E_{\theta 2}^{d}(\theta) = -E_0 V_B^{i,r}\left(\frac{\mathrm{w}}{2}, \xi_2, n = 2\right)\frac{e^{-j\beta r_2}}{r_2} \tag{1.14b}$$

where

$$\xi_2 = \psi_2 = \begin{cases} \frac{\pi}{2} - \theta & 0 \le \theta \le \frac{\pi}{2} \\ \frac{5\pi}{2} - \theta & \frac{\pi}{2} \le \theta \le \pi \end{cases} \tag{1.15}$$

For far-field observations, the radial distances can be reduced to

$$\left.\begin{aligned} r_1 &\simeq r - \frac{\mathrm{w}}{2}\cos\left(\frac{\pi}{2} - \theta\right) = r - \frac{\mathrm{w}}{2}\sin\theta \\ r_2 &\simeq r + \frac{\mathrm{w}}{2}\cos\left(\frac{\pi}{2} - \theta\right) = r + \frac{\mathrm{w}}{2}\sin\theta \end{aligned}\right\} \quad \text{for phase terms}$$

$$r_1 \simeq r_2 \simeq r \qquad \text{for amplitude terms} \tag{1.16}$$

Therefore the diffracted fields can be represented by

$$E^d_{\theta 1}(\theta) = +E_0 V_B^{i,r}\left(\frac{\mathrm{w}}{2}, \theta + \frac{\pi}{2}, n = 2\right) e^{j(\beta \mathrm{w}/2)\sin\theta} \frac{e^{-j\beta r}}{r} \tag{1.17}$$

$$E^d_{\theta 2}(\theta) = -E_0 V_B^{i,r}\left(\frac{\mathrm{w}}{2}, \xi_2, n = 2\right) e^{-j(\beta \mathrm{w}/2)\sin\theta} \frac{e^{-j\beta r}}{r} \tag{1.18}$$

Figures 1.8 and 1.9 are the comparisons of the results, for a monopole on square and circular ground planes of FEKO (the black solid line) and the author's program (the red dashed line) using GO and GTD/UTD. The monopole is operating at 1 GHz ($\lambda \approx 0.3$ m). The width of the square ground plane and the diameter of the circular plate is 1.22 meters ($\mathrm{w} = a \approx 4\lambda$).

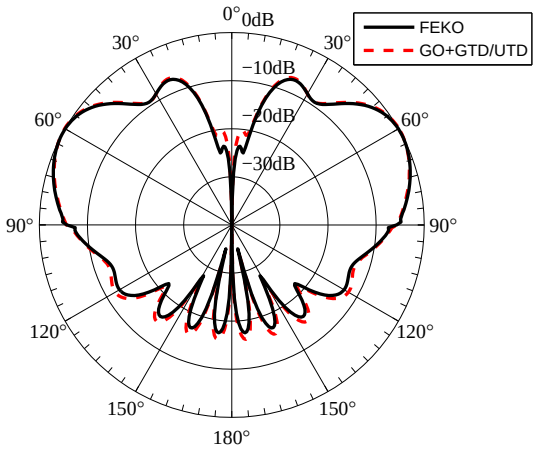

Figure 1.8: The normalized radiation pattern comparison of FEKO and author's program for the square ground plane case.

Radiation patterns of a monopole above a square PEC ground plane are illustrated in Figure 1.8. FEKO's result is based on UTD. The author's pattern is obtained from GO and two-point wedge diffraction (first-order) theory. A very good agreement is deserved between the FEKO and GO + GTD patterns. Small discontinuities occur at 90° on the pattern of UTD, because FEKO only account for first-order diffractions.

There are high-order diffractions between the edges, which are not accounted in the modeling and simulations by FEKO. The discontinuities exist also in author's pattern, however, they are less significant comparing to those by FEKO.

For the monopole mounted on a circular ground plane, shown in Figure 1.2 (b), the GO fields are the same as the patterns of a monopole mounted above a square plane. However, the edge of the ground plane is curved. Therefore, to account for the radii of curvature of incident and reflected waves, the amplitude spreading factors are revised and they are represented, respectively, for edges #1 and #2 by [6]

$$A_1(r_1, a) = \frac{1}{r_1}\sqrt{\frac{a}{\sin\theta}} \simeq \frac{1}{r}\sqrt{\frac{a}{\sin\theta}} \tag{1.19a}$$

$$A_2(r_2, a) = \frac{1}{r_2}\sqrt{-\frac{a}{\sin\theta}} \simeq \frac{1}{r}\sqrt{-\frac{a}{\sin\theta}} \tag{1.19b}$$

Therefore the diffracted fields for the circular ground plane can ultimately be written as

$$E^d_{\theta 1}(\theta) = +E_0 V_B^{i,r}\left(a, \theta + \frac{\pi}{2}, n = 2\right)\frac{e^{j\beta a\sin\theta}}{\sqrt{\sin\theta}}\frac{e^{-j\beta r}}{r} \qquad \theta_0 \le \theta \le \pi - \theta_0 \tag{1.20}$$

$$E^d_{\theta 2}(\theta) = -E_0 V_B^{i,r}\left(a, \xi_2, n = 2\right)\frac{e^{-j\beta a\sin\theta}}{\sqrt{-\sin\theta}}\frac{e^{-j\beta r}}{r} \qquad \theta_0 \le \theta \le \pi - \theta_0 \tag{1.21}$$

where

$$\xi_2 = \psi_2 = \begin{cases} \frac{\pi}{2} - \theta & \theta_0 \le \theta \le \frac{\pi}{2} \\ \frac{5\pi}{2} - \theta & \frac{\pi}{2} \le \theta \le \pi - \theta_0 \end{cases} \tag{1.22}$$

Figure 1.9 is the comparison of the circular PEC ground plane case. Since the rim of the circular ground plane acting as a "ring radiator" [6], the diffracted fields become singular at the symmetry axis ($\theta = 0^\circ$ and 180°). In addition to GTD/UTD, the author's diffracted radiation pattern near the symmetry axis ($\theta_0 = 12^\circ$) is computed using equivalent currents [6].

$$E^d(r) = j\pi a E_0\left[V_B^{i,r}(a, \psi = \xi_1, n = 2)\right] J_1(\beta a\sin\theta)\frac{e^{-j\beta r}}{r} \qquad \begin{cases} 0 \le \theta \le \theta_0 \\ \pi - \theta_0 \le \theta \le \pi \end{cases} \tag{1.23}$$

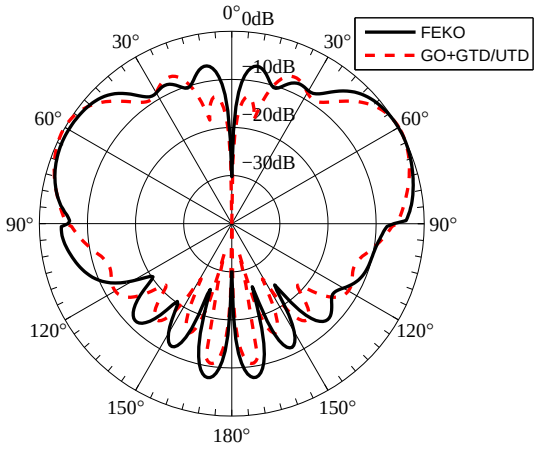

Figure 1.9: The normalized radiation pattern comparison of FEKO and author's program for the circular ground plane case.

However, FEKO's UTD results exhibit significant discontinuities and it is not symmetric. This is caused by an incorrect meshing provided by FEKO's default setting. It is hard to obtain an accurate prediction for a more complex geometry using the UTD based on the current meshing method of FEKO.

1.3 The Blade Antennas

The two blade antennas were manufactured by **Spectrum Antenna & Avionics Systems (P) ltd.** of Cochin, India. According to the manufacturer's literature, the C-band antenna operates over a frequency range of 5.4 GHz to 5.9 GHz, making the center frequency 5.65 GHz. It will generally be referred to here as "the C-band antenna." The other antenna's operating frequency is from 2.35 GHz to 2.45 GHz, which will be referred as "the S-band antenna." The input impedance of both antennas is 50 ohms, with a maximum VSWR of 1.5 : 1.

The two antennas are very similar to each other. They have identical bases and

(a) (b)

Figure 1.10: Photographs of the blade antennas. (a) The C-band antenna. (b) The S-band antenna.

mounting hole patterns, they are both fed by female SMA (SubMiniature version A) connectors, the blades of both are tilted aft by approximately 37°, and they both have an asymmetrical diamond aerodynamic cross section. The only significant visual difference between them is the height of the blade which is 25 mm for the C-band antenna and 44 mm for the S-band case. A photograph of the C-band antenna is shown in Figure 1.10 (a) while that of the S-band antenna is illustrated in Figure 1.10 (b).

Figures 1.11, 1.12 and 1.13 are the measured radiation patterns of both S-band and C-band blade antennas in the roll plane, pitch plane and yaw plane. The radiation pattern of the S-band antenna achieves its maximum value of 4.25 dB at $\theta = 48°$. According to Figure 1.13, the S-band pattern in the yaw plane is omnidirectional. The patterns in the roll and pitch planes resembles those of a quarter-wavelength wire antenna mounted on the circular ground plane. However, the C-band case is more complicated. Its roll plane and pitch plane patterns have conspicuous differences. As seen in Figure 1.13, the yaw-plane pattern of the C-band antenna deviates significantly from omnidirectional.

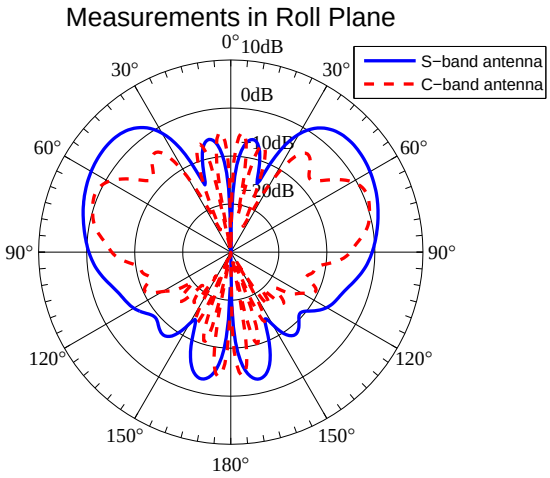

Figure 1.11: The $\phi = 90°$ elevation-plane pattern (the roll plane) of the blade antennas mounted on the 13″ diameter ground plane.

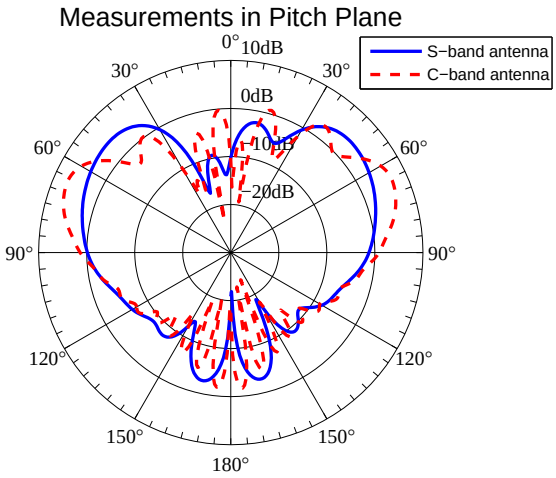

Figure 1.12: The $\phi = 0°$ elevation-plane pattern (the pitch plane) of the blade antennas mounted on the 13″ diameter ground plane.

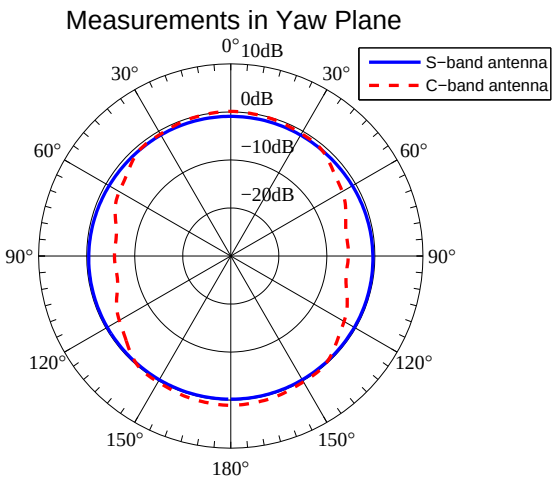

Figure 1.13: The azimuth-plane pattern (the yaw plane) of the blade antennas mounted on the 13″ diameter ground plane.

Figure 1.14 shows the return loss of the blade antennas mounted on a 48″ diameter circular ground plane, Figure (a) is for the S-band antenna and Figure (b) is the C-band case. According to the manufacture's descriptions, the operational frequency range of the S-band blade antenna is between 2.35 GHz and 2.45 GHz. The C-band blade antenna operates from 5.4 GHz to 5.9 GHz. The frequency range of the measurements is much broader than the antennas' operating frequency bands.

As shown in Figure 1.14 (a), the resonant frequency occurs at 2.4 GHz, which is the center frequency of the S-band blade antenna as indicated in the manufacture's descriptions. It is lower than −20 dB within the operating frequency. However, the return loss of the C-band antenna is not similar to the typical case. The return loss is below −16 dB within the working frequency. It has a potential of operating from 5.4 GHz to 6.8 GHz, which is twice the bandwidth described.

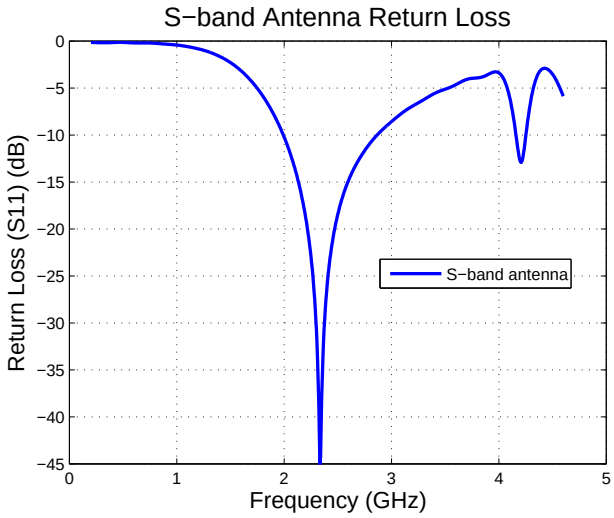

(a)

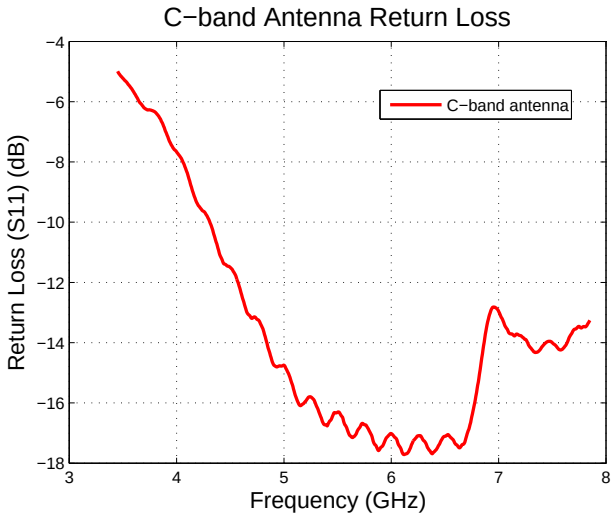

(b)

Figure 1.14: The return loss of the blade antennas mounted on a 48″ diameter circular ground plane. (a) S-band antenna. (b) C-band antenna.

1.4 Models in Simulation Codes

Overall, five different models were made from scratch in both FEKO and WIPL-D (some are made in WIPL-D Pro, the others are made in WIPL-D Pro CAD). They are the Hypothetic Model, the Base-Part-Added Model, the X-Ray-Based Model, the Reasonable-Approximation Model and the Dissection-Based Model. Each model is more complicated than the previous model and is modified based on the previous one, except the Dissection-Based Model. The last model is built according to the anatomic features of the antenna that were revealed when its radome was removed.

The models are simulated in FEKO and WIPL-D with the method of moments (MoM) for Integral Equations (IE). These models provide different levels of accuracy and computational efficiency. They can be selectively implemented into other models, for instance helicopter models, by user's demands.

There are two criteria for the models: radiation patterns and return loss (indicated in the last section). They are used to judge if the model is a good approximation of the antenna. Several questions arose when building the models: the type of material of the dielectric cover, structure of the radiation elements, methods of the matching circuits.

These models are introduced in the following chapter.

1.5 FEKO

FEKO is a product of EM Software & Systems-S.A. (Pty) Ltd. (EMSS-SA). It is a comprehensive electromagnetic simulation software tool with different numerical methods, including Method of Moments (MoM), Geometrical Optics (GO), Physical Optics (PO), Uniform Theory of Diffraction (UTD), Finite Element Method (FEM) and Multi-level Fast Multipole Method (MLFMM) [2].

When creating CAD geometries, FEKO provides canonical structures and supports boolean operations. This feature provides a convenient way of building complicated $3D$ models.

Users are allowed to select the methods of creating mesh (surface and volume meshes) from CAD geometries: adjusting the size of mesh or utilizing the suggested selections.

FEKO is a volume-based simulation software. For instance, users are allowed to set the properties of the surface and volume separately, which is not possible in WIPL-D Pro.

1.6 WIPL-D Pro

WIPL-D Pro is a product of WIPL-D d.o.o., a privately-owned company dedicated to development of commercial EM software.

Other than FEKO, the only numerical methods of WIPL-D Pro is the Method of Moments (MoM). Meanwhile, it introduces quadrilateral mesh and high-order basis functions (HOBFs). It is addressed in the introduction of WIPL-D Pro, "MoM, quad-mesh and HOBFs significantly decrease required number of unknowns and memory requirements for simulation [3]." With numbers of simulations, the execution time of simulations in WIPL-D Pro is significantly shorter than those of FEKO.

When creating CAD geometries, WIPL-D Pro does not support boolean operations. This becomes an obstacle for users building complicated $3D$ models in WIPL-D Pro.

The mesh size is adjustable in WIPL-D Pro as well. However, only surface meshes are created, which could be the reason of the high computational efficiency of WIPL-D Pro.

Unlike FEKO, WIPL-D Pro is based on modeling of surfaces between volumes and

not volumes instead. The properties of volumes are defined by their boundaries. It implies that the existence of boundaries between consecutive volumes with the same properties are not allowed.

1.7 WIPL-D Pro CAD

WIPL-D Pro CAD is another product of WIPL-D d.o.o..

WIPL-D Pro CAD is a combination of WIPL-D Pro's kernel and a more powerful modeling tool. The numerical method of WIPL-D Pro CAD is the same as that of WIPL-D Pro, which is the Method of Moments (MoM). It is a surface-based simulation software, which is the same as WIPL-D Pro. However, WIPL-D Pro CAD supports boolean operations and provides more canonical structures. These make modeling complex geometries more convenient [4].

The computational efficiencies of WIPL-D Pro and WIPL-D Pro CAD are in the same level, which is much higher than that of FEKO.

Chapter 2

MODELS IN SIMULATION CODES

In this chapter, the five simulation models of the blade antennas are discussed. Their predicted radiation patterns and return losses are compared with measurements. The radiation patterns are compared in the three principal planes. The return losses are compared over a wider frequency range than the operating range. The C-band antenna operates over a frequency range of 5.4 GHz to 5.9 GHz, the S-band antenna's operating frequency is from 2.35 GHz to 2.45 GHz.

2.1 The Hypothetic Model

As shown in Figures 2.1 and 2.5, the Hypothetic Model is built in FEKO and WIPL-D Pro with the same size. These simple models include only the dielectric blade part and the radiation element. The blade part of the model is solid with an assumed dielectric constant of 3.5. A tilted quarter-wavelength thin wire is inside the blade part, which forms a quarter-wavelength monopole inside a dielectric cover. The monopole is parallel to the shell of the radome.

As Shown in Figures 2.2, 2.3 and 2.4, the predicted (both FEKO and WIPL-D) principal-plane radiation patterns are compared with measurements. These predicted radiation patterns agree very well with the measured patterns.

Based on the simulations, several conclusions are formed.

- The radiating element in these blade antennas can be modeled (very well) as a tilted $\frac{\lambda}{4}$ monopole.
- To compare favorably with measurements, the modeled monopole may be tilted aft by approximately 37°.

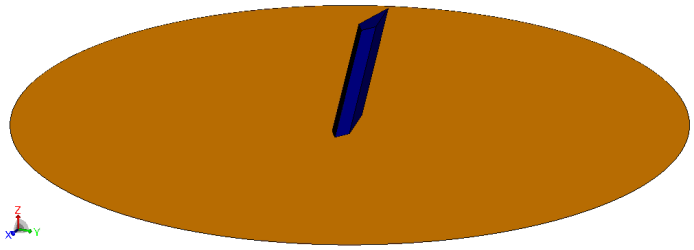

(a)

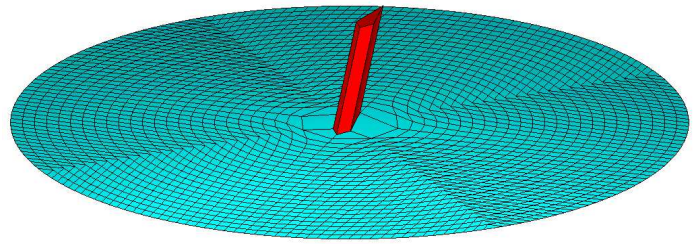

(b)

Figure 2.1: The Hypothetic S-band blade antenna models mounted on a 13″ diameter circular ground plane. (a) Top view of the model in FEKO. (b) Top view of the model in WIPL-D.

- The WIPL-D- and FEKO-simulated patterns for the 2.4 GHz antenna system are nearly identical.

However, the radiation patterns of the C-band antenna needs to be looked at more closely. The measured pattern in the azimuthal plane is not omnidirectional, and the deviation from omni is close to 6 dB.

Figure 2.5 are Hypothetic Models of the C-band blade antenna in FEKO and WIPL-D. Figures 2.6, 2.7 and 2.8 are simulation results of these hypothetic models compared to the measurements.

Figure 2.7 gives a fine simulation result of the pitch plane. However in Figure 2.6, the predicted gain is greater than the measurement by around 5 dB. The yaw-plane results in Figure 2.4 are omnidirectional, in contrast to the measured pattern.

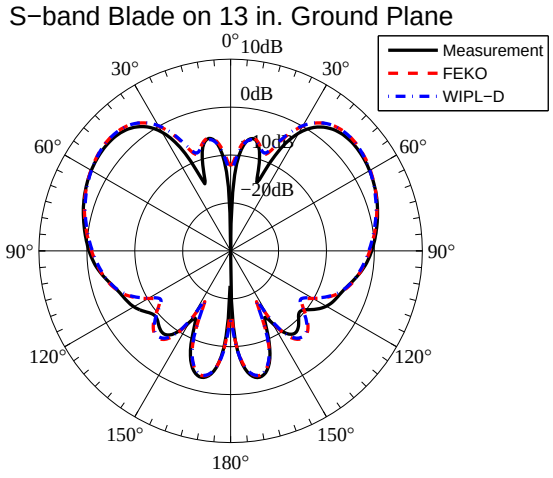

Figure 2.2: The $\phi = 90°$ elevation-plane pattern (the roll plane) of the S-band blade antenna mounted on the 13″ diameter ground plane. Compare the measurement with **the Hypothetic Model** in FEKO and WIPL-D.

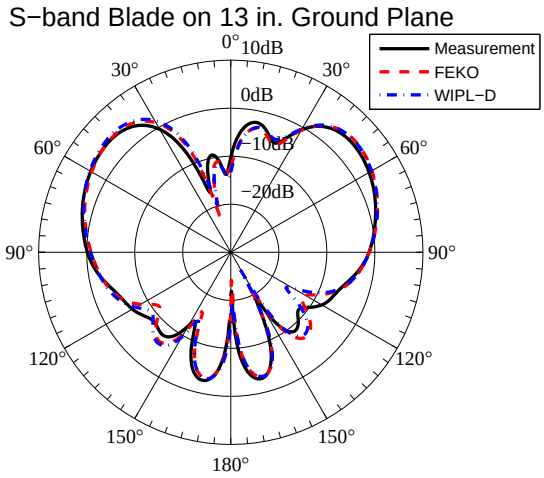

Figure 2.3: The $\phi = 0°$ elevation-plane pattern (the pitch plane) of the S-band blade antenna mounted on the 13″ diameter ground plane. Compare the measurement with **the Hypothetic Model** in FEKO and WIPL-D.

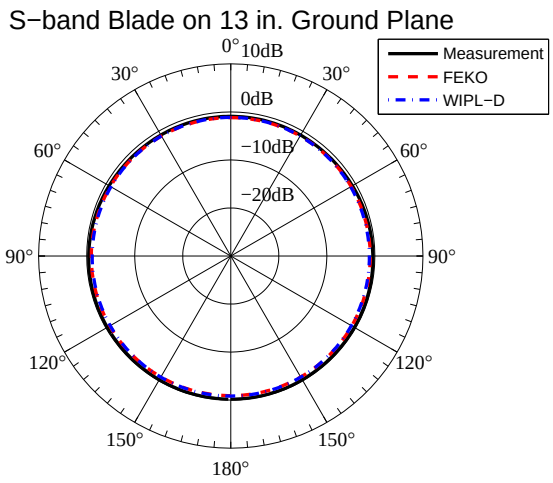

Figure 2.4: The azimuth-plane pattern (the yaw plane) of the S-band blade antenna mounted on the 13″ diameter ground plane. Compare the measurement with **the Hypothetic Model** in FEKO and WIPL-D.

The predicted radiation patterns for the S-band antenna using the Hypothetic Model (the radiating element is modeled as a simple quarter wavelength wire) agree very well with the measurements. However, the C-band predictions do not agree very well with measurements. Therefore, additional efforts will concentrate somewhat on the C-band antenna until this enigma is resolved.

2.2 The Base-Part-Added Model

Historically, this model was developed prior to receiving the X-rays of the antennas. It was evident from an external examination of the antenna that its construction includes a dielectric covered aluminum base plate, which is referred as the "base part." This dielectric covered plate extends the entire length of the base of the antenna, and a limit on its height could also be determined. With this new part included in the model (Figure 2.9), a much improved agreement between simulations and measure-

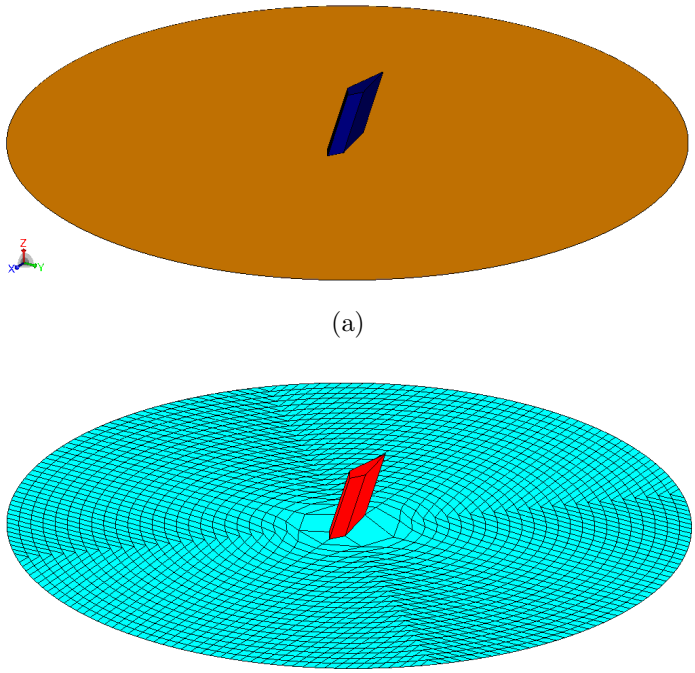

(a)

(b)

Figure 2.5: The Hypothetic C-band blade antenna models mounted on a 13″ diameter circular ground plane. (a) Top view of the model in FEKO. (b) Top view of the model in WIPL-D.

ments of the C-band blade antenna was obtained (Figures 2.10, 2.11 and 2.12). It is clear from these results that the presence of the base part is responsible for the deviation from omnidirectional of the C-band antenna. With several modifications to the model, it turns out to be that the aluminum plate hardly has an impact to the radiation patterns, therefore the dielectric cover is the major reason for the deviation.

Based on the simulation results, the relative permittivity (ϵ_r) of the dielectric cover is set to be 3.5 to obtain a good agreement with measurement. For the computational efficiency, the aluminum plate is unnecessary to exhibit in the model for an accurate radiation pattern prediction. It seems curious that the presence of the whole base

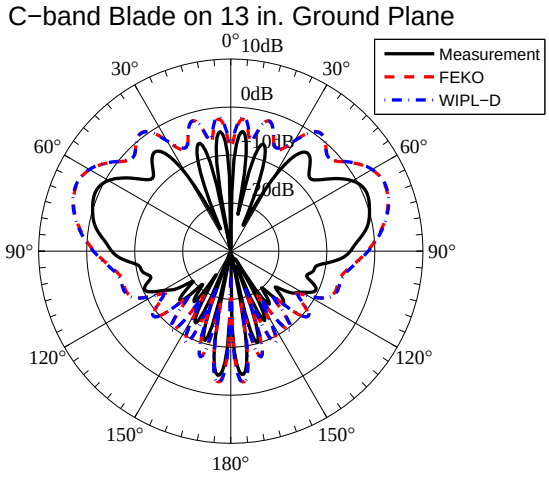

Figure 2.6: The $\phi = 90°$ elevation-plane pattern (the roll plane) of the C-band blade antenna mounted on the 13″ diameter ground plane. Compare the measurement with **the Hypothetic Model** in FEKO and WIPL-D.

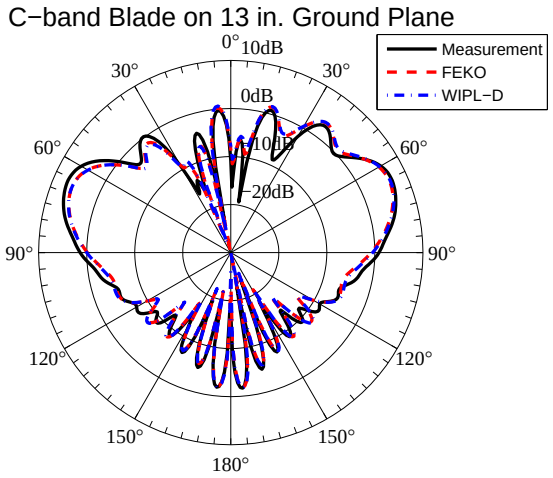

Figure 2.7: The $\phi = 0°$ elevation-plane pattern (the pitch plane) of the C-band blade antenna mounted on the 13″ diameter ground plane. Compare the measurement with **the Hypothetic Model** in FEKO and WIPL-D.

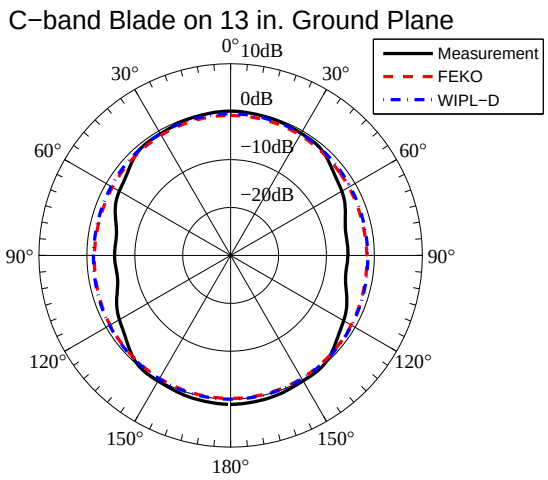

Figure 2.8: The azimuth-plane pattern (the yaw plane) of the C-band blade antenna mounted on the 13″ diameter ground plane. Compare the measurement with **the Hypothetic Model** in FEKO and WIPL-D.

part does not have an impact on the S-band patterns.

2.3 Return Loss

In Figure 2.13, the predicted return loss based on the Hypothetic Model is compared with the measured return loss of the C-band antenna. It is clear that a simple monopole is insufficient to accurately model the antenna's input characteristics. In particular, there is no relative null, or even a reasonably good match, within the antenna's operating range of 5.4 GHz to 5.9 GHz. The Base-part-added Model has a similar simulation result in return loss with the Hypothetic Model.

The type of matching circuits inside the antennas must be figured out.

At this point in our story, the X-rays of the antennas had arrived. A munificence from Boeing, Mesa. A much more detailed model of the antenna was now possible (Figures 2.14 and 2.25). Still concentrating on the C-band antenna, the X-Ray-Based

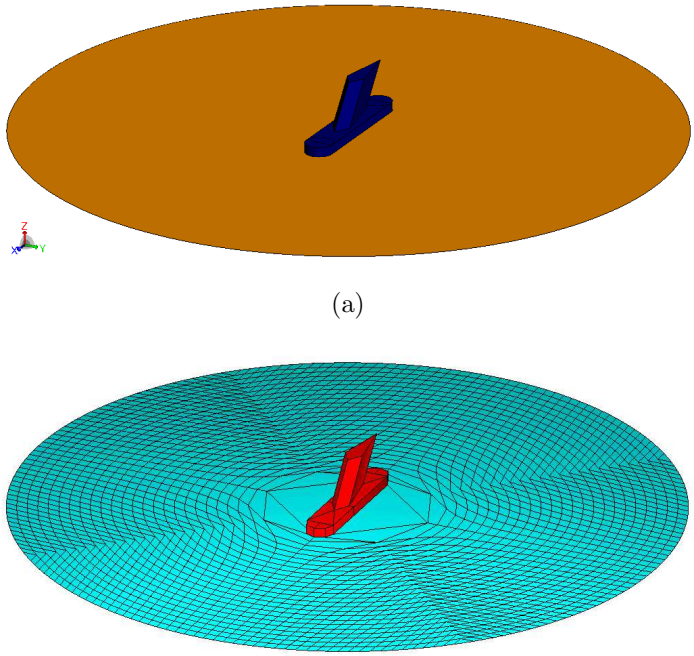

(a)

(b)

Figure 2.9: Base-part-added C-band blade antenna models mounted on a 13″ diameter circular ground plane. (a) Top view of the model in FEKO. (b) Top view of the model in WIPL-D.

Model was developed. It includes all of the metallic structures previously hidden within the radome, as shown in Figure 2.15. Since the presence of the coil that is connected from the radiating element and the ground for ESD protection has been found to be problematic with respect to the radiation patterns (in the next page or two of this thesis), the return loss of the C-band antenna is predicted with and without this element.

When the wire coil is included in the simulation model, a good match occurs in the prediction near the center frequency of the antenna's operating band of 5.65 GHz. However, the frequency response of the predicted return loss is quite different from the measured one, as seen in Figure 2.17. When that coil is removed from the model,

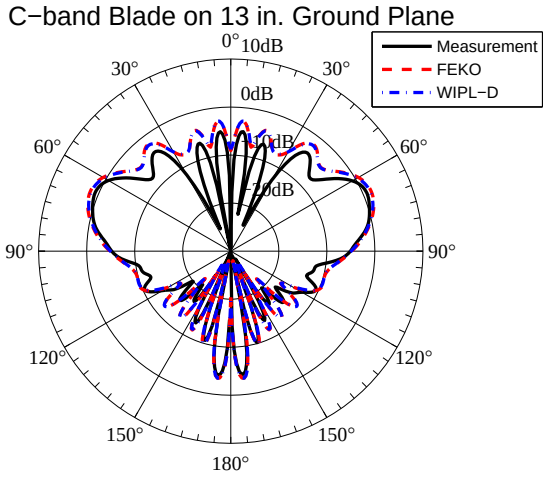

Figure 2.10: The $\phi = 90°$ elevation-plane pattern (the roll plane) of the C-band blade antenna mounted on the 13″ diameter ground plane. Compare the measurement with **the Base-part-added Model** in FEKO and WIPL-D.

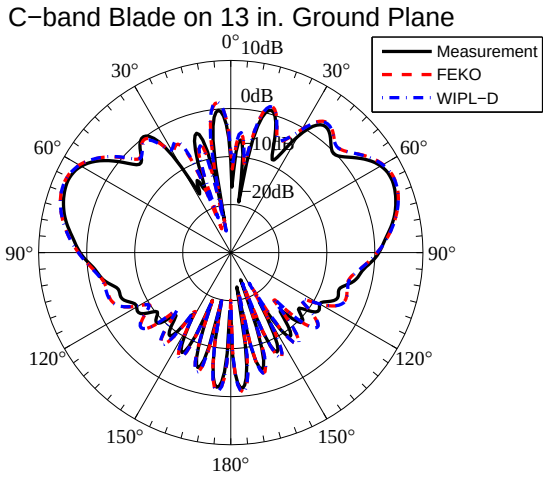

Figure 2.11: The $\phi = 0°$ elevation-plane pattern (the pitch plane) of the C-band blade antenna mounted on the 13″ diameter ground plane. Compare the measurement with **the Base-part-added Model** in FEKO and WIPL-D.

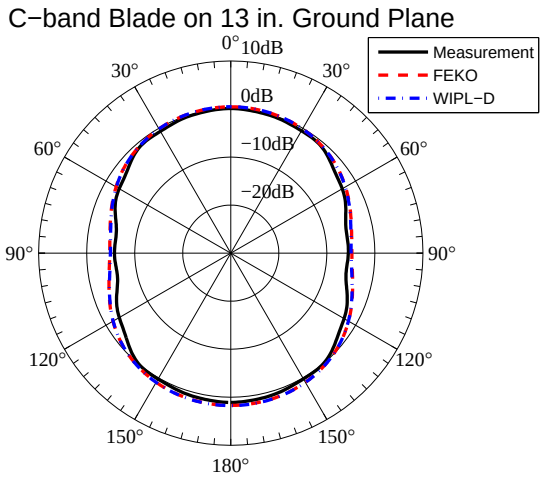

Figure 2.12: The azimuth-plane pattern (the yaw plane) of the C-band blade antenna mounted on the 13″ diameter ground plane. Compare the measurement with **the Base-part-added Model** in FEKO and WIPL-D.

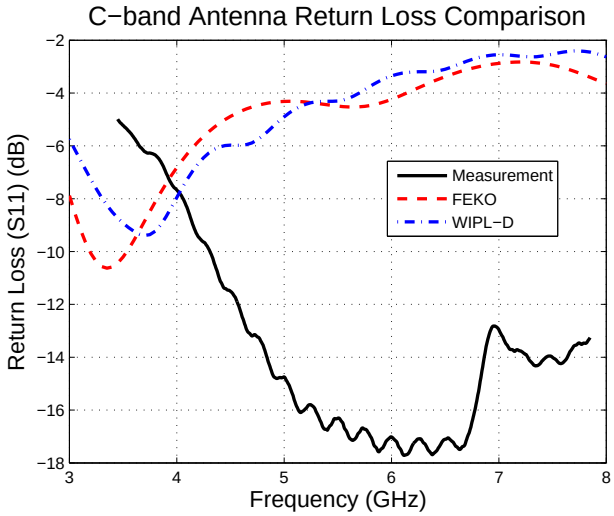

Figure 2.13: The return loss for the C-band blade antenna, measurement compared with the simplified models of FEKO and WIPL-D showed in Figure 2.5.

Figure 2.14: A close-cropped view of the X-ray of the C-band antenna.

not only is the predicted frequency response dissimilar to that measured, there is no match within the operating band (Figure 2.18).

2.4 The X-Ray-Based Model

The FEKO-predicted radiation patterns of the X-Ray-Based Model of the C-band antenna are compared with their measured counterparts in Figures 2.19, 2.20 and 2.21. This is the complete model that includes the coil that is connecting the antenna element and the ground, which is a metal plate of the SMA adaptor, as shown in Figure 2.15 (a). The presence of the coil has a profound impact on the predicted radiation patterns.

In Figures 2.22, 2.23 and 2.24, the principal-plane patterns predicted by FEKO using the same model but with the coil removed (Figure 2.15 (b)) are compared with measurements. These predicted patterns are much closer to the measurements than those which included the coil.

The opinion of our colleague John Fenick of Trivec Avant was solicited concerning these results. John indicated that he has also experienced inaccuracies when attempting to model small coils. He suggested that a strong current is flowing through the coil in the simulation that does not exist in the physical antenna. Clearly, the coil is present in the physical antenna and yet the measured radiation patterns are well

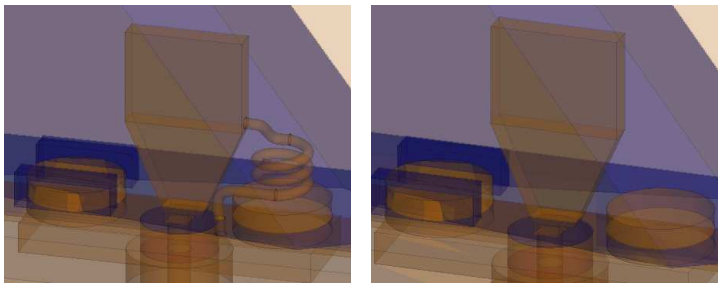

(a) (b)

Figure 2.15: Radiation elements of the X-Ray-Based C-band blade antenna models in FEKO. (a) The model with the coil part. The coil connects to the radiating element and ground. (b) The model without the coil.

behaved. This supports John's contention that the simulation of the coil is in error.

From the comparison between Figures 2.17 and 2.18, it leads to a conclusion that the coil is part of the matching circuit. However, the matching method is more like a single-point matching. The coil does not provide a bandwidth as wide as the measurement. At this time point, the importance of the size of the coil has not been noticed.

2.5 The Reasonable-Approximation Model

The complete X-Ray-Based Model for the S-band antenna is shown in Figure 2.26 (a). Since the antenna dimensions are known to a relatively high degree of precision, predicting the return loss of the S-band antenna is a way to infer a better estimate of the relative dielectric constant of the antenna's radome.

The measured return loss of the S-band blade exhibits a single deep null. If the dimensions of the simulation model are identical to the physical model, then the

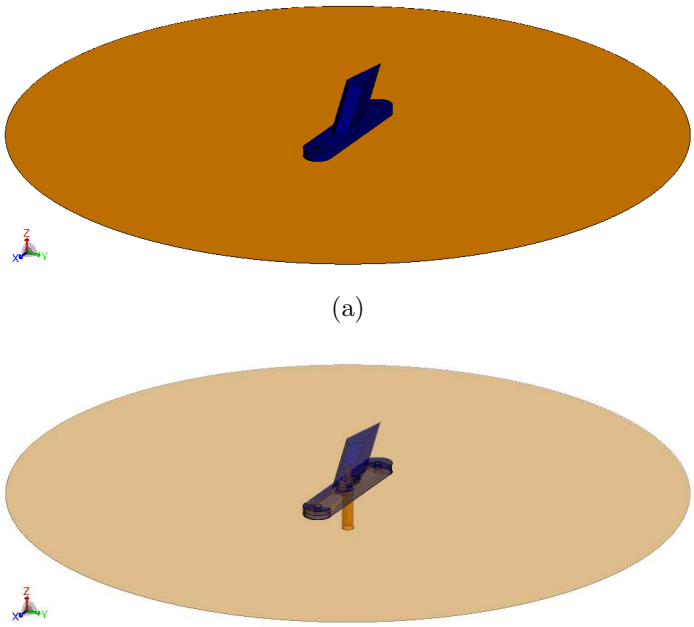

(a)

(b)

Figure 2.16: X-Ray-Based C-band blade antenna models mounted on a 13″ diameter circular ground plane. (a) Top view of the model in FEKO. (b) Top view of the model in FEKO with an opacity of 60%.

frequency at which the predicted null in the return loss occurs will be a function of the permittivity of the radome.

2.5.1 Relative Permittivity of the Radome

In the previous models, the relative dielectric constant ϵ_r of the radome was set to be 3.5. This assumption is acceptable for radiation patterns. However, the relative permittivity of the radome is one of the dominant factors to the input impedance characteristics. A better estimate of ϵ_r of the radome is important for developing a more complete model.

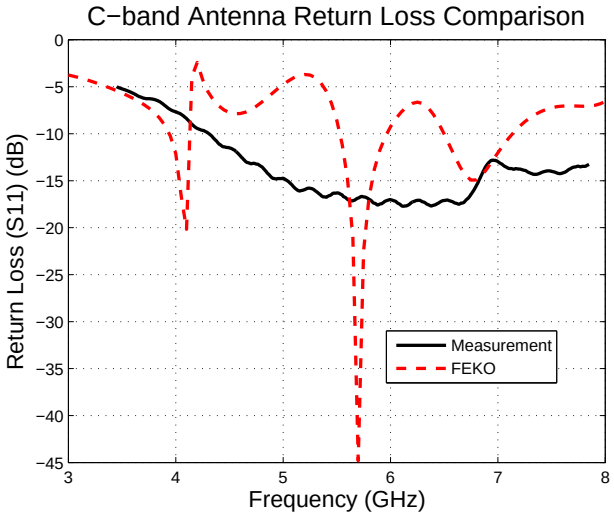

Figure 2.17: The return loss for the C-band blade antenna, measurement compared with the X-Ray-Based Models of FEKO, with the coil connected, shown in Figure 2.15 (a).

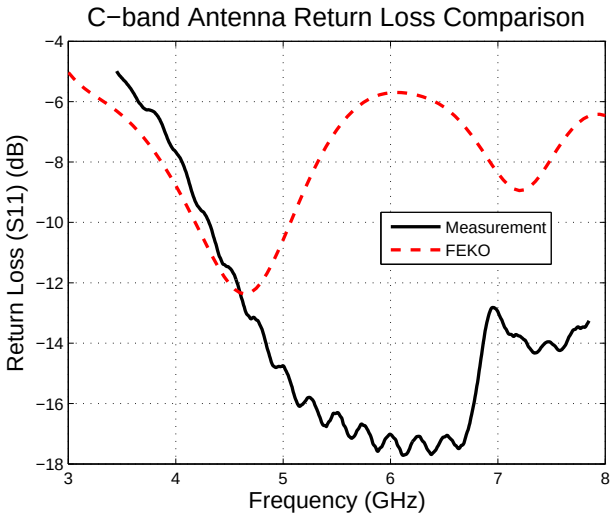

Figure 2.18: The return loss for the C-band blade antenna, measurement compared with the X-Ray-Based Models of FEKO, the coil is removed, shown in Figure 2.15 (b).

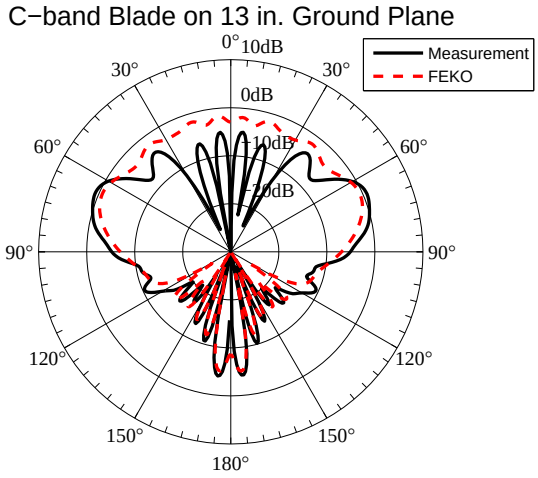

Figure 2.19: The $\phi = 90°$ elevation-plane pattern (the roll plane) of the C-band blade antenna mounted on the 13″ diameter ground plane. Compare the measurement with the X-Ray-Based model in FEKO, with the coil connected, shown in Figure 2.15 (a).

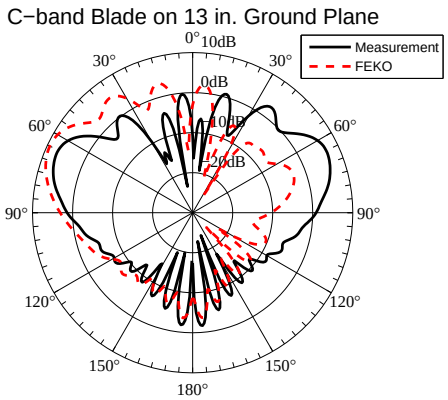

Figure 2.20: The $\phi = 0°$ elevation-plane pattern (the pitch plane) of the C-band blade antenna mounted on the 13″ diameter ground plane. Compare the measurement with the X-Ray-Based model in FEKO, with the coil connected, shown in Figure 2.15 (a).

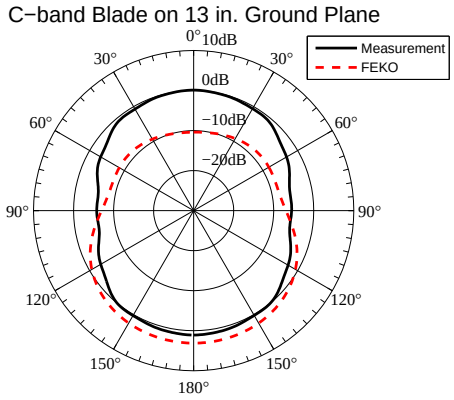

Figure 2.21: The azimuth-plane pattern (the yaw plane) of the C-band blade antenna mounted on the 13″ diameter ground plane. Compare the measurement with the X-Ray-Based model in FEKO, with the coil connected, shown in Figure 2.15 (a).

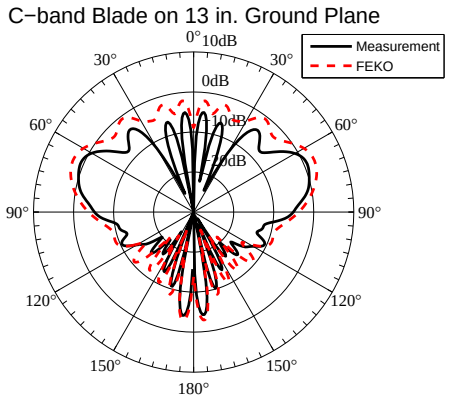

Figure 2.22: The $\phi = 90°$ elevation-plane pattern (the roll plane) of the C-band blade antenna mounted on the 13″ diameter ground plane. Compare the measurement with the X-Ray-Based model in FEKO, the coil is removed, shown in Figure 2.15 (b).

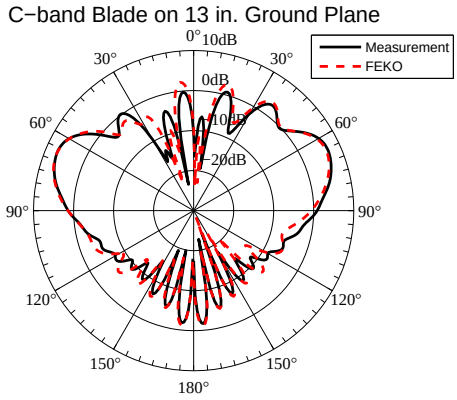

Figure 2.23: The $\phi = 0°$ elevation-plane pattern (the pitch plane) of the C-band blade antenna mounted on the 13″ diameter ground plane. Compare the measurement with the X-Ray-Based model in FEKO, the coil is removed, shown in Figure 2.15 (b).

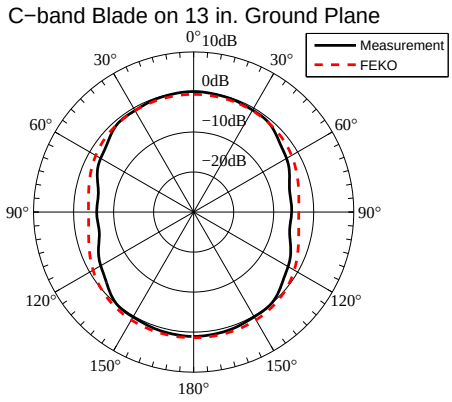

Figure 2.24: The azimuth-plane pattern (the yaw plane) of the C-band blade antenna mounted on the 13″ diameter ground plane. Compare the measurement with the X-Ray-Based model in FEKO, the coil is removed, shown in Figure 2.15 (b).

Figure 2.25: A close-cropped view of the X-ray of the S-band antenna.

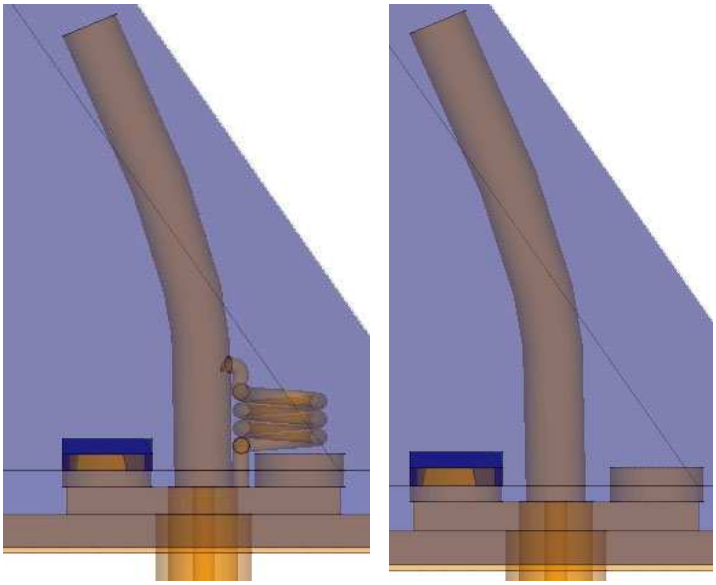

(a) (b)

Figure 2.26: Side view of the X-Ray-Based Model of S-band antennas. Modeled by FEKO. (a) With the coil. (b) With the coil removed.

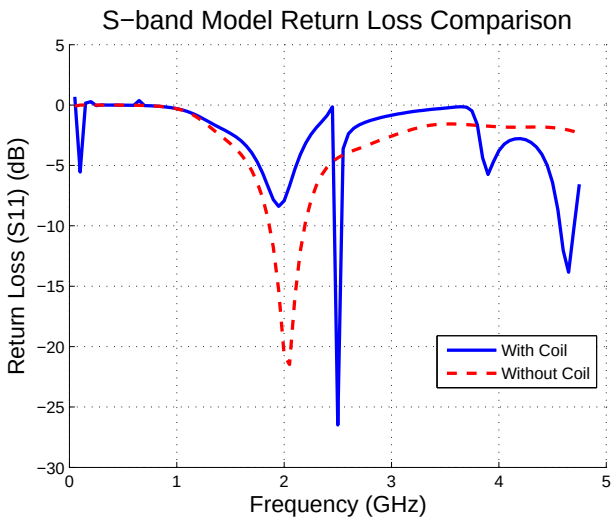

Figure 2.27: The return loss comparison between the X-Ray-Based Model with and without the wire coil.

Figure 2.27 is a comparison of two X-Ray-Based Models of the S-band blade antenna which are identical in dimensions: one with the coil, the other one with the coil removed (shown in Figure 2.26). A logical conclusion based on the measurements, and simulations performed with and without the coils, is that the purpose of the coil is ESD/lightening protection. Although they are clearly present in the physical antennas, the predicted radiation patterns are much closer to those measured when the coils are removed from the models. Although we do not fully understand why, there is a significant current in the simulated coils that is not present in the physical coils. Therefore the coil was removed from the S-band model for this return loss prediction. Without the erroneous influence of the coil, the assumed relative permittivity of 3.5 for the radome corresponds to a resonant frequency of approximately 2 GHz. However, the measured return loss of the S-band blade antenna exhibits a single deep null at 2.4 GHz. By adjusting the permittivity of the radome several times such that the null in the predicted return loss occurs at 2.4 GHz, a more accurate estimate of

ϵ_r was found to be 1.95.

2.5.2 The Reasonable-Approximation Model of the S-band Antenna

In contrast to the C-band antenna case, the simulation results of radiation patterns of the S-band X-Ray-Based Model are very close to the measurements.

Figure 2.28 is the Reasonable-Approximation Model of the S-band Antenna in FEKO and WIPL-D. As shown in Figures 2.29, 2.30 and 2.31, simulation results of the radiation patterns of the S-band Reasonable-Approximation Model in FEKO and WIPL-D have a very good agreement with the measurements in the principal planes. The S-band Reasonable-Approximation Model also predicts a deep null in the return loss curve at the frequency at which the null of the measurement occurs.

Based on comparisons of simulation results and measurements, FEKO and WIPL-D have a very good agreement in this S-band antenna model. Their accuracies are at the same level. However, WIPL-D does have a much shorter running time.

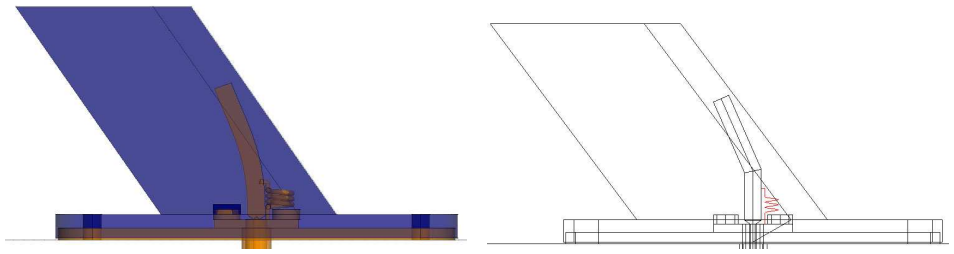

(a) (b)

Figure 2.28: Reasonable-Approximation **S-band** blade antenna models mounted on a 13″ diameter circular ground plane. (a) Side view of the model in FEKO. (b) Side view of the model in WIPL-D.

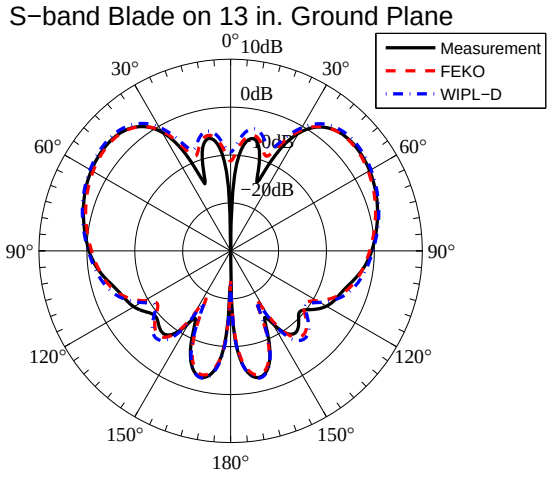

Figure 2.29: The $\phi = 90°$ elevation-plane pattern (the roll plane) of the **S-band** blade antenna mounted on the 13″ diameter ground plane. Compare the measurement with **the Reasonable-Approximation Model** in FEKO and WIPL-D.

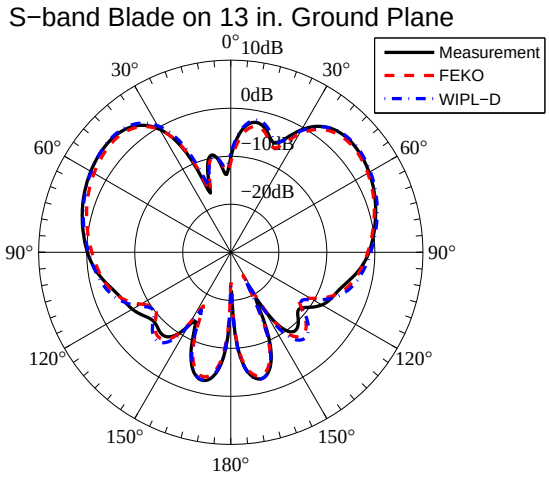

Figure 2.30: The $\phi = 0°$ elevation-plane pattern (the pitch plane) of the **S-band** blade antenna mounted on the 13″ diameter ground plane. Compare the measurement with **the Reasonable-Approximation Model** in FEKO and WIPL-D.

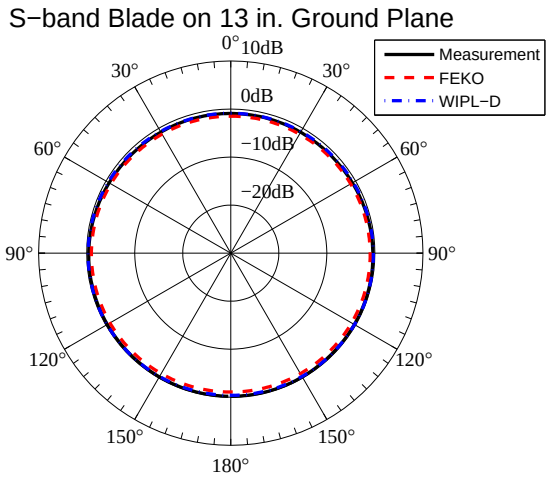

Figure 2.31: The azimuth-plane pattern (the yaw plane) of the **S-band** blade antenna mounted on the 13″ diameter ground plane. Compare the measurement with **the Reasonable-Approximation Model** in FEKO and WIPL-D.

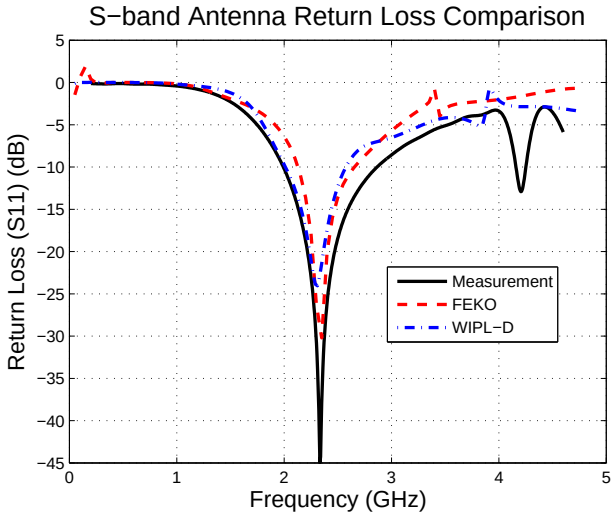

Figure 2.32: The return loss for the **S-band** blade antenna, measurement compared with **the Reasonable-Approximation Models** of FEKO and WIPL-D

2.5.3 *The Reasonable-Approximation Model of the C-band Antenna*

Figure 2.33 shows the simulation results of current distributions of the S- and C-band X-Ray-Based Models. Clearly, the current on the coil part of the C-band model is exceptionally high. This graph proves the previous assumption in the Former Conclusions section that the coil in C-band antenna was not modeled correctly.

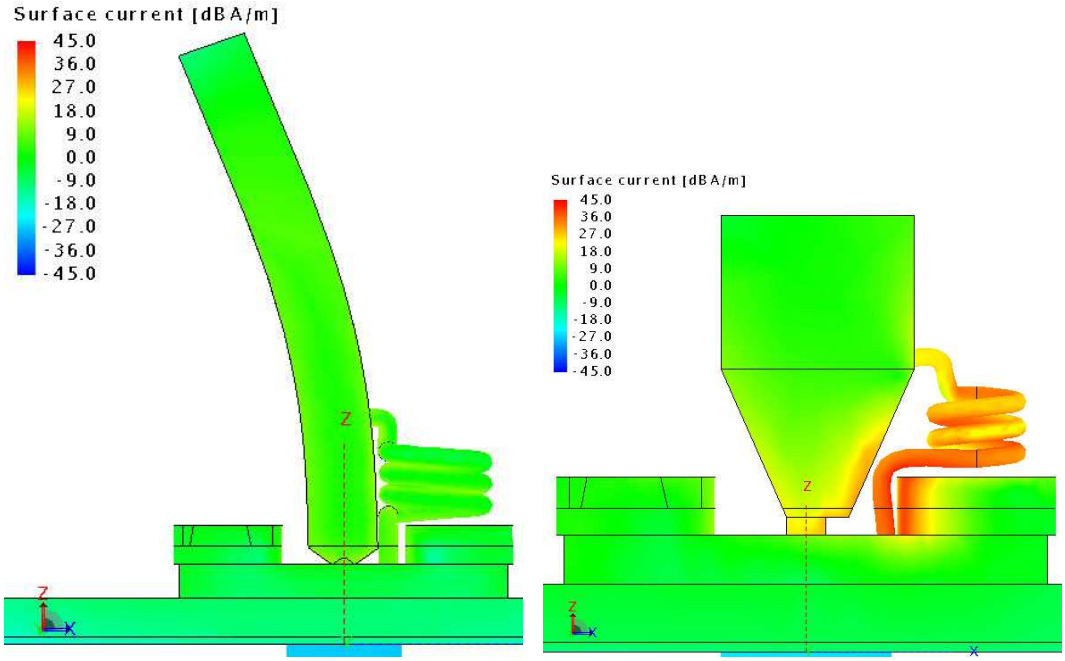

(a) (b)

Figure 2.33: Current distribution plots of the X-Ray-Based Model in FEKO. (a) Current distribution of the S-band antenna (b) Current distribution of the C-band antenna.

After several experimental modifications to the coil part (by changing its location, connection joint, cross section, etc.), the dominant factor of the current issue was found. The radius (or the dimension of the cross section) is important to the model's performance. There is a threshold of the coil dimension for the C-band model. The

coil's dimension must be smaller than a certain criterion (in this case, the diameter of the coil should be equal or less than 2 mm) to obtain accurate radiation pattern predictions. The radius of the coil of the C-band X-Ray-Based Model was beyond the threshold, which led to a significant distortion.

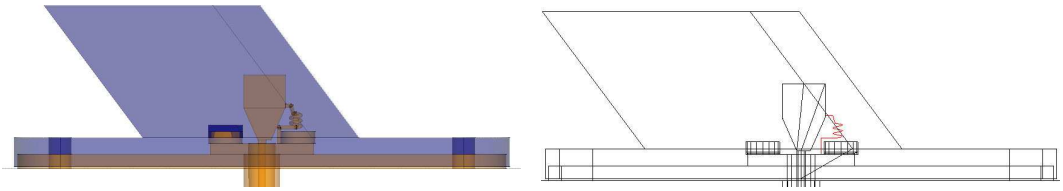

(a) (b)

Figure 2.34: Reasonable-Approximation **C-band** blade antenna models mounted on a 13″ diameter circular ground plane. (a) Side view of the model in FEKO. (b) Side view of the model in WIPL-D.

By adjusting the radius of the coil (Figure 2.34), the C-band Reasonable-Approximation Model was developed. It exhibits good agreement with the measurement in the pitch plane (Figure 2.36), around 3 dB difference in roll and yaw planes. There remains significant discrepancies between the measured and predicted return losses. Although the measured return loss curve of the C-band antenna is suspiciously anomalous, its shape has been verified by measuring a different copy of the antenna. While the shapes of the predicted return loss curves do not resemble the measurement, they do exhibit a null at approximately 5.65 GHz which is the center frequency of the C-band blade antenna (Figure 2.38).

2.6 The Dissection-Based Model

To approach more accurate predictions of C-band antenna radiation patterns, the interior structure of the C-band antenna need to be investigated. The predictions of

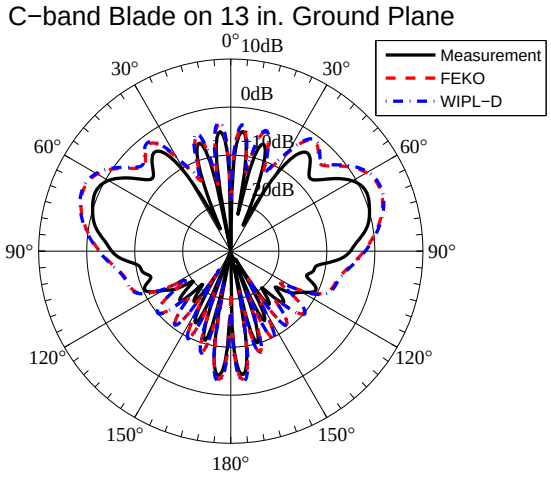

Figure 2.35: The $\phi = 90°$ elevation-plane pattern (the roll plane) of the **C-band** blade antenna mounted on the 13″ diameter ground plane. Compare the measurement with **the Reasonable-Approximation Model** in FEKO and WIPL-D.

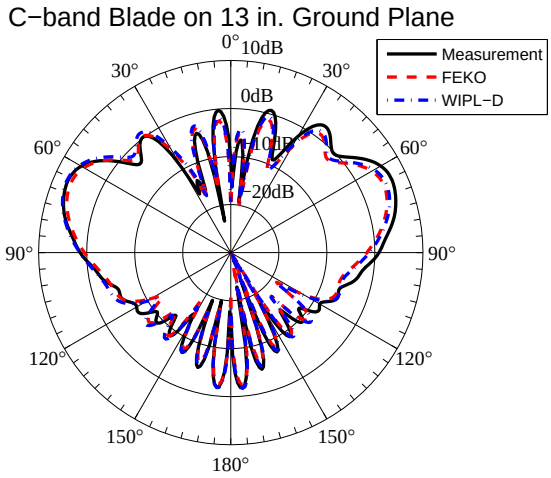

Figure 2.36: The $\phi = 0°$ elevation-plane pattern (the pitch plane) of the **C-band** blade antenna mounted on the 13″ diameter ground plane. Compare the measurement with **the Reasonable-Approximation Model** in FEKO and WIPL-D.

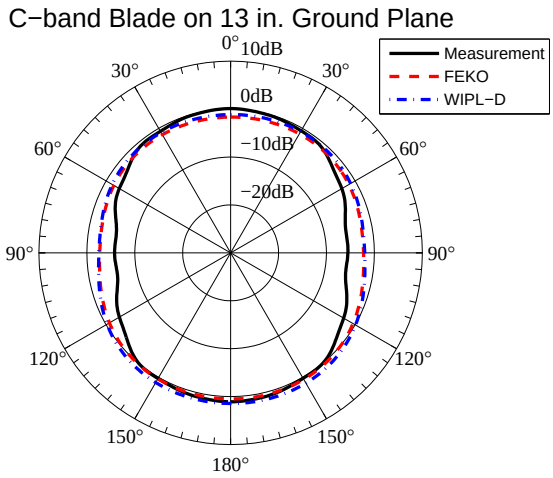

Figure 2.37: The azimuth-plane pattern (the yaw plane) of the **C-band** blade antenna mounted on the 13″ diameter ground plane. Compare the measurement with **the Reasonable-Approximation Model** in FEKO and WIPL-D.

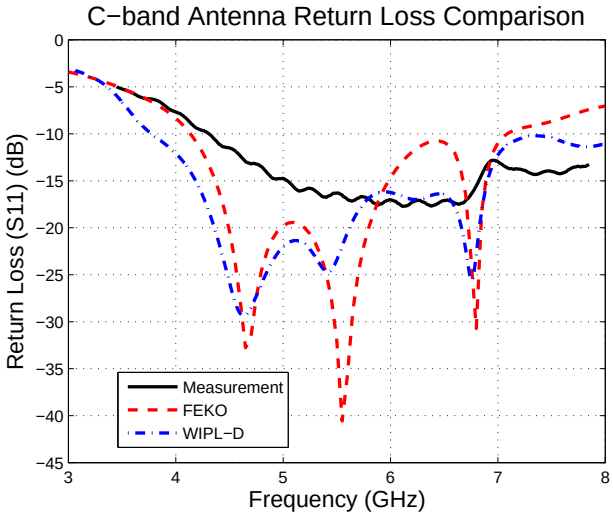

Figure 2.38: The return loss for the **C-band** blade antenna, measurement compared with **the Reasonable-Approximation Model** of FEKO and WIPL-D

the C-band antenna exhibit significant discrepancies to the measurements. A reasonable assumption is that there are subtle differences between the existing prediction model and the physical antenna that are not detectable in the X-ray image. To test this assumption, the antenna was dissected — that is, the radome was removed.

Figure 2.39 shows the interior structure of the C-band antenna. Contrary to previous beliefs, the metallic structures of the antenna are not encapsulated in dielectric material. The blade part is a hollow cavity around the radiation element. The blade part has a uniform thickness of approximately 3% wavelength. The sense of rotation of the coil is incorrect in the previous model. From Figure 2.39 (b), it is seen that the flat of the radiation element is not parallel to the pitch plane. Instead, it is rotated by approximately 10°. Furthermore, the dimensions of the element in the X-Ray-Based Model were slightly in error due to this rotation. In addition, the thickness of the element was now known.

With several modifications according to dissection figures, new models built in FEKO and WILP-D Pro CAD are shown in Figure 2.40. The antenna is fed by a coaxial cable. It consists of a blade-shaped shell, a radiation element, an SMA connector with two screw nuts and the base part with screw holes. These screw holes do not have strong impacts on the radiation patterns nor on the return loss. The dielectric blade part has a thickness of 3% wavelength. It forms a cavity inside the dielectric cover. The radiation element is in vacuum not surrounded by the dielectric material. Another modification is made on the relative permittivity of the shell. It is set to be 4.5 since the manufacturer claims the shell is vacuum molded from single-piece glass.

As shown in Figure 2.42, the simulated radiation pattern in the pitch plane does not have a conspicuous change. Meanwhile, results in the roll plane (Figure 2.41) and yaw plane (Figure 2.43) are improved. Results from FEKO and WIPL-D Pro

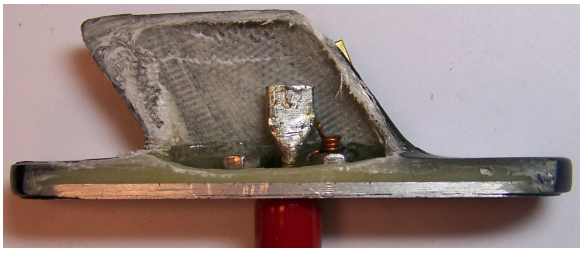

(a)

(b)

Figure 2.39: Photographs of the dissected **C-band** blade antenna. (a) Side view. (b) Top view.

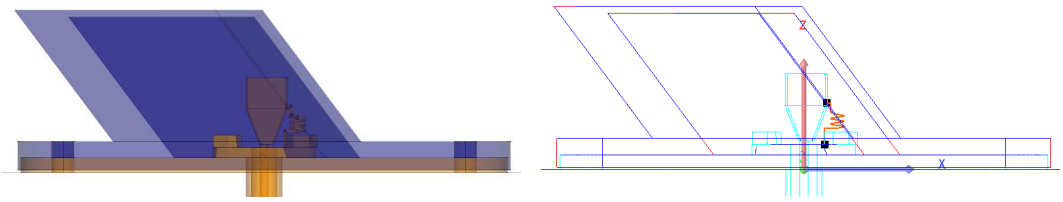

(a) (b)

Figure 2.40: Dissection-Based **C-band** blade antenna models mounted on a 13″ diameter circular ground plane. (a) Side view of the model in FEKO. (b) Side view of the model in WIPL-D.

CAD overlap with the measurements in most directions. Two differences in roll plane remain. One is that several deep nulls (lower than −30 dB) exist in the measurement near the zenith direction. The other difference is the lower amplitude of the measurement at approximately ±100°. These differences may be caused by slight differences in shape of the dielectric cover. They can be neglected in most cases. In conclusion, the radiation simulation results of the Dissection-Based Model exhibits good agreement with the measurements.

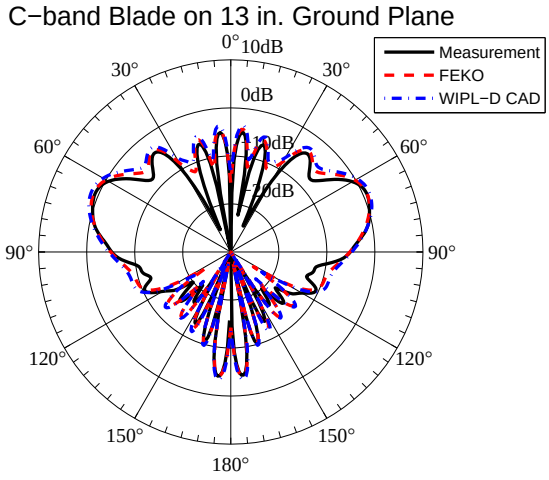

Figure 2.41: The $\phi = 90°$ elevation-plane pattern (the roll plane) of the **C-band** blade antenna mounted on the 13″ diameter ground plane. Compare the measurement with **the Dissection-Based Model** in FEKO and WIPL-D.

There still remains significant discrepancies between the measured and predicted return losses. The simulation result from FEKO does not change much over the operating range, which is 5.4 to 5.9 GHz. It retains the deep null at the center frequency. The simulated return loss of WIPL-D increases for around 6 dB comparing with the result of Reasonable-Approximation Model. It seems the Dissection-Based Model has a worse return loss prediction than the previous model. The return losses

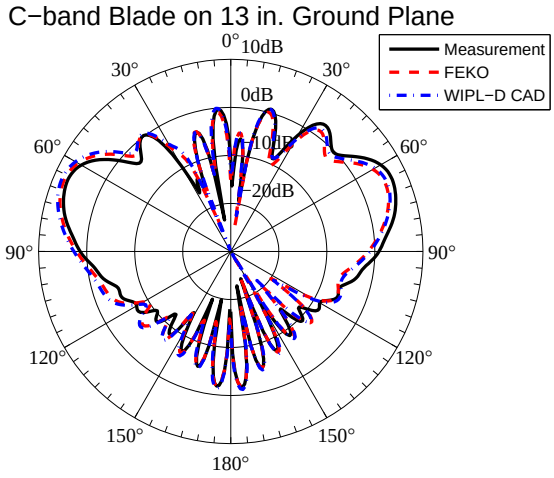

Figure 2.42: The $\phi = 0°$ elevation-plane pattern (the pitch plane) of the **C-band** blade antenna mounted on the 13″ diameter ground plane. Compare the measurement with **the Dissection-Based Model** in FEKO and WIPL-D.

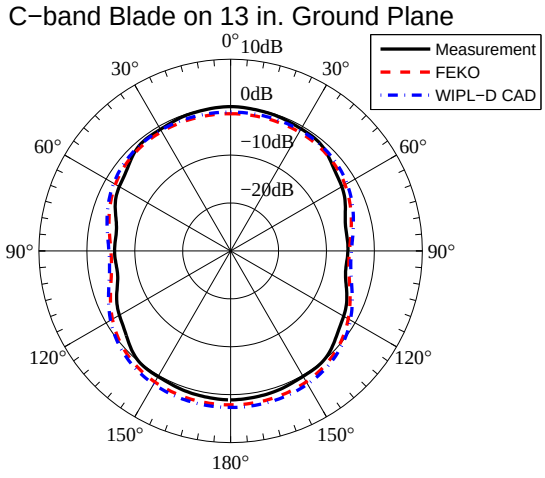

Figure 2.43: The azimuth-plane pattern (the yaw plane) of the **C-band** blade antenna mounted on the 13″ diameter ground plane. Compare the measurement with **the Dissection-Based Model** in FEKO and WIPL-D.

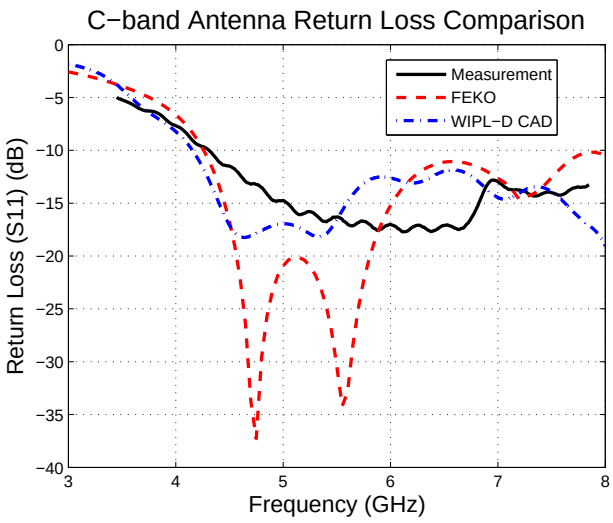

Figure 2.44: The return loss for the **C-band** blade antenna, measurement compared with with **the Dissection-Based Model** of FEKO and WIPL-D

are shown in Figure 2.44.

Chapter 3

CONCLUSIONS, SUMMARY AND FUTURE WORK

3.1 Conclusions and Summary

Early simulation models of the blade antennas, consisting of a simple quarter-wavelength monopole and dielectric radome (The Hypothetic Model), result in predicted radiation patterns which agree quite well with measurements. The reason that the C-band antenna exhibits a nearly 6 dB deviation from omnidirectional turns out to be the influence from the dielectric radome's base. Both the relative permittivity and the dimensions of the base part make a difference in the radiation pattern, particularly in the yaw plane.

With the availability of the X-rays of the antennas, courtesy of Ron Lavin of Boeing Helicopters, Mesa, developing a more detailed simulation model became possible. The initial X-Ray-Based Model of the C-band antenna has strikingly distorted radiation patterns. The incorrect dimension of the coil is the dominant reason for the observed phenomena. There is a threshold for the size of the coil part. Beneath the threshold, the size of the coil would only affect the input impedance characteristics.

By modifications of the radome and coil, the Reasonable-Approximation Model is obtained. The S-band Reasonable-Approximation Model exhibits very good agreement with the measurements. The radiation patterns in the principal planes are almost identical to the measurements. Similarly, the predicted and measured return losses are in good agreement.

The C-band predictions do not fare quite as well. While the amplitude of the roll-plane patterns are significantly higher than that of the measurement over the

upper hemisphere, the FEKO and WIPL-D predicted patterns are nearly identical to one another. There is good agreement in the pitch plane, but the amplitude of the predicted yaw-plane patterns are somewhat high in the left and right side directions (but, again, identical to one another). The measured return loss for the C-band antenna is very strange, and the predicted return loss curves do not resemble the measurement. However, the shapes of the measured return loss curves of two nominally identical C-band antennas are very similar to one another.

With the Dissection-Based Model, the C-band radiation patterns results improved. The blade part became hollow (vacuum) inside. The relative permittivity of the dielectric cover is set to be 4.5. With these two modifications, the radiation patterns have a very good agrement in all three principal planes. Changing the sense of rotation of the coil and slightly rotating the radiation element do not make a difference to the simulation results. This model does not improve the prediction accuracy of the return loss compared to the previous model. The computational efficiency of the Reasonable-Approximation and Dissection-Based Models are similar to each other. The execution time for these two detailed models is significantly longer than those of the earlier models.

In terms of accuracy of the prediction results, it is the opinion of this author that FEKO and WIPL-D Pro are comparable. However, WIPL-D Pro runs faster than FEKO, and it has smaller memory requirements. FEKO has an edge over WIPL-D in terms of the ease with which geometries are modeled. However, WIPL-D has significantly narrowed that edge by introducing WIPL-D Pro CAD. Pro CAD has enhanced modeling capabilities, such as Boolean algebra, that are similar to those of FEKO.

In summary:

- The Hypothetic S-band Model provides very well radiation patterns with a

high time efficiency. The Base-Part-Added C-band Model gives good radiation predictions and have a high computational efficiency as well.

- The Reasonable-Approximation Model of the S-band antenna provides accurate radiation patterns and return loss.

- The Dissection-Based C-band Model of WIPL-D Pro CAD has the closest return loss prediction. The Reasonable-Approximation Model of the C-band antenna has better radiation patterns.

- WIPL-D (either WIPL-D Pro or WIPL-D Pro CAD) always runs faster than FEKO with the same model. However, it is more convenient building models with FEKO.

3.2 Future Work

The models have provided accurate predictions of radiation patterns. Models with higher computational efficiency in FEKO need to be developed. The return loss prediction of the C-band blade antenna is still not sufficiently accurate. With a better insight of the antenna, a more accurate model of the impedance characteristics could be developed. It would also be interesting to develop more efficient models while the accuracy remains at the same level.

FEKO presents different methods of solving the fields. However, the GO and UTD in FEKO do not predict the requested fields correctly. More investigations are needed for the different solver's codes provided by FEKO.

REFERENCES

[1] "Aircraft rotations", www.grc.nasa.gov/WWW/K-12/airplane/rotations.html (2008).

[2] "Overview of feko", www.feko.info/product-detail/overview-of-feko (2013).

[3] "Overview of wipl-d pro", www.wipl-d.com/products.php?cont=wipl-d-pro (2013).

[4] "Overview of wipl-d pro cad", www.wipl-d.com/products.php?cont=wipl-d-pro-cad (2013).

[5] Balanis, C. A., *Antenna Theory: Analysis and Design* (John Wiley & Sons, 2005), 3rd edn.

[6] Balanis, C. A., *Advanced Engineering Electromagnetics* (John Wiley & Sons, 2012), 2nd edn.

[7] Keller, J. B., "Geometrical theory of diffraction", J. Opt. Soc. Am. **52**, 2, 116 – 130 (1962).

[8] Kozakoff, D. J., *Analysis of Radome Enclosed Antennas* (Artech House, 2009), 2nd edn.

[9] M.Weiner, M., *Monopole Antennas* (Taylor & Francis, 2003).

[10] Pathak, P., "A uniform geometrical theory of diffraction for an edge in a perfectly conducting surface", Proc. IEEE **62**, 11, 1448 – 1461 (1974).